International Union of Pure and Applied Chemistry

REPRINTED FROM

Molecular Electronics

A 'Chemistry for the 21st Century' Monograph

ISBN 0-632-04284-2

EDITED BY

J. JORTNER & M. RATNER

Blackwell
Science

9 Optical Properties of Semiconductor Nanocrystals (Quantum Dots)

D.J. NORRIS,* M.G. BAWENDI† and L.E. BRUS‡

*Department of Chemistry and Biochemistry, University of California, San Diego, 9500 Gilman Drive, La Jolla, CA 92093-0340, USA,

†Department of Chemistry, Massachusetts Institute of Technology, 77 Massachusetts Avenue, Cambridge, MA 02139, USA,

‡Department of Chemistry, Columbia University, 3000 Broadway, New York, NY 10027, USA

1 Introduction

One possible route to 'molecular electronics' is to incorporate molecular-like behaviour in standard semiconductor materials. This approach has led to the investigation of nanometre-scale semiconductor structures over the past several decades. Interest in new opto-electronic materials has driven the development of thin semiconductor sheets (quantum wells), narrow rods (quantum wires), and nanometre-scale crystallites (quantum dots). Absorption of a photon by these materials promotes an electron from the valence band into the conduction band, creating an electron–hole pair. When the size of these semiconductor structures is comparable to or smaller than the natural length scale of the electron–hole pair, it is confined in one (wells), two (wires), or all three dimensions (dots). The spatial confinement leads to interesting molecular-like optical behaviour as the motion of the carriers is quantized by the boundary of the material. Since these materials are structurally identical to the bulk crystal, these properties arise solely due to their finite size. This phenomenon, known as the 'quantum size effect', is both fundamentally and practically important. An investigation of these quantum structures addresses a size-regime intermediate between molecular and solid-state behaviour. In addition it may lead to unique properties for potential applications.

Due to the complete confinement of the carriers, the quantum size effect is the most dramatic in quantum dots. When a semiconductor nanocrystal is embedded in an insulating material, as illustrated in Fig. 9.1, the photoexcited carriers reside in a potential well in all three dimensions and the conduction and valence bands are quantized due to the finite size of the dot [1–3]. In contrast to the bulk absorption spectrum, which is a continuum above the band gap of the semiconductor (E_g^s) [4], quantum dot spectra exhibit a series of discrete electronic transitions. Because of this behaviour these materials are sometimes referred to as 'artificial atoms'. Since the energies of the transitions are affected by the amount of confinement, the optical spectra of quantum dots are also strongly dependent on the size of the crystallite.

In this chapter we address the optical properties of semiconductor quantum dots and discuss recent developments in understanding their basic photophysics. Two prototypical quantum dot systems are described. First, in Section 2 the absorption and emission behaviour of cadmium selenide (CdSe) dots are discussed. Due to significant advances in fabrication methods [5], CdSe is now one of the most well understood quantum dot materials. Extremely high quality CdSe dots can be produced and much new information has been obtained for this system. We begin Section 2 by describing the basic

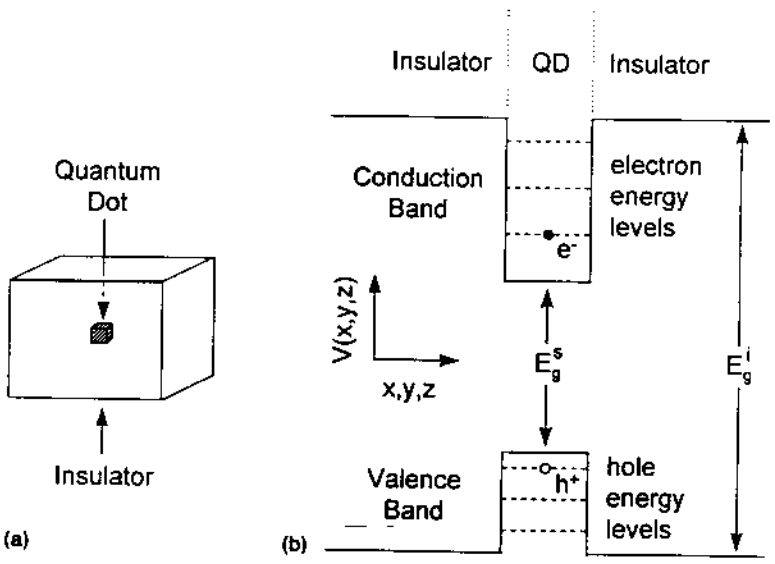

Figure 9.1 (a) Quantum dot (QD) structure. A nanometre-scale semiconductor crystallite is embedded inside an insulating material. (b) Potential well formed in any one dimension (x, y, or z) in the conduction and valence bands. The energy levels of the excited carriers (electrons and holes) become quantized due to the finite size of the semiconductor.

concepts necessary to understand the optical properties of CdSe quantum dots. We then address two long-standing questions in strongly confined quantum dot systems:

1 the size dependence of the optical spectrum;
2 the origin of the long-lived luminescence.

Second, in Section 3 we discuss the optical properties of silicon (Si) quantum dots. These dots are particularly interesting not only because of silicon's technological significance, but also because Si, in contrast to CdSe, is an indirect gap semiconductor. In such materials, optical transitions at the band gap are dipole forbidden and occur only via less efficient vibrationally assisted processes [4]. However, since this selection rule arises due to the long-range translational symmetry of the bulk material, it is modified in finite size dots where translational invariance is no longer valid. Therefore, band gap absorption and luminescence become weakly dipole-allowed in Si quantum dots. The possibility that Si quantum dots might be a useful optical material has attracted widespread interest, especially in connection with the quantum and luminescence properties of porous Si thin films made by electrochemical etching. In Section 3 our present imperfect understanding of these systems is discussed.

2 CdSe quantum dots

2.1 *Basic concepts*

2.1.1 'PARTICLE-IN-A-SPHERE'

For direct gap semiconductor quantum dots such as CdSe much of the basic photophysics can be explained by the simple 'particle-in-a-sphere' model [1–3]. This model

considers an arbitrary particle of mass m_0 inside a spherical potential well of radius a.

$$V(r) = \begin{cases} 0 & r < a \\ \infty & r > a. \end{cases} \tag{9.1}$$

Following Flügge [6], the Schrödinger equation is solved yielding wavefunctions

$$\Phi_{n,l,m}(r, \theta, \phi) = C \frac{j_l(k_{n,l}r)Y_l^m(\theta, \phi)}{r}, \tag{9.2}$$

where C is a normalization constant, $Y_l^m(\theta, \phi)$ is a spherical harmonic, $j_l(k_{n,l}r)$ is the lth order spherical Bessel function, and

$$k_{n,l} = \frac{\alpha_{n,l}}{a} \tag{9.3}$$

with $\alpha_{n,l}$ the nth zero of j_l. The energy of the particle is given by

$$E_{n,l} = \frac{\hbar^2 k_{n,l}^2}{2m_0} = \frac{\hbar^2 \alpha_{n,l}^2}{2m_0 a^2}. \tag{9.4}$$

Due to the symmetry of the problem the eigenfunctions (Eqn 9.2) are simple atomic-like orbitals which can be labelled by the quantum numbers n(1, 2, 3. . .), l(s, p, d. . .), and m. The energies (Eqn 9.4) are identical to the kinetic energy of the free particle, except that the wavevector, $k_{n,l}$, is quantized by the spherical boundary condition. Note also that the energy is proportional to $1/a^2$ and therefore is strongly dependent on the size of the sphere.

At first glance, this model may not seem useful for the quantum dot problem. The particle above is confined to an empty sphere, while the quantum dot is filled with semiconductor atoms! However, by a series of approximations the quantum dot problem can be reduced to the 'particle-in-a-sphere' form (Eqn 9.1). The photoexcited carriers (electrons and holes) may then be treated as particles inside a sphere of constant potential.

First, the bulk conduction and valence bands are approximated by simple isotropic bands within the effective mass approximation [7]. According to Bloch's theorem, the bulk wavefunctions can be written as

$$\Psi_{nk}(\mathbf{r}) = u_{nk}(\mathbf{r})\exp(i\mathbf{k}\cdot\mathbf{r}) \tag{9.5}$$

where u_{nk} is a function with the periodicity of the crystal lattice and the wavefunctions are labelled by the band index n and wavevector $\mathbf{k}$. The energy of these wavefunctions are typically described in a 'band diagram', a plot of E vs $\mathbf{k}$. Although band diagrams are in general quite complex and difficult to calculate, in the effective mass approximation the bands are assumed to have simple parabolic forms near extrema in the band diagram. For example, since CdSe is a direct gap semiconductor, both the valence band maximum and conduction band minimum occur at $k = 0$ (see Fig. 9.2). In the effective mass approximation, the energy of the conduction (n = c) and valence (n = v) bands are approximated as

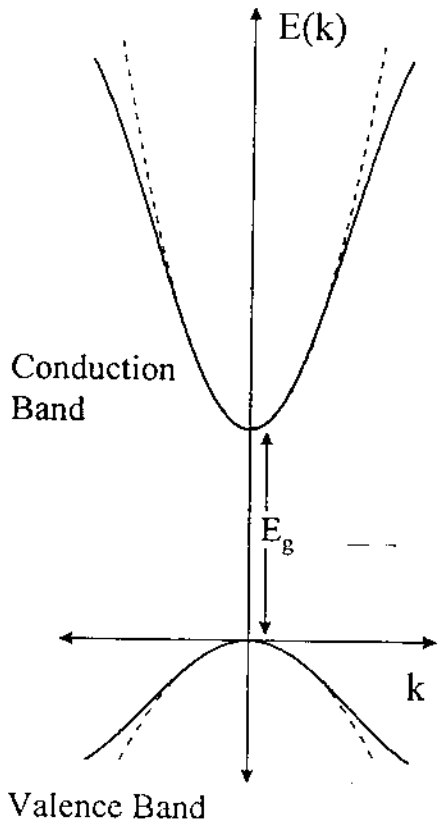

Figure 9.2 Simple two-band model for bulk direct gap semiconductors. The real band structure (solid lines) is approximated by parabolic bands (dashed lines) at $k = 0$ in the effective mass approximation. The curvature of the bands reflects the 'mass' of the electrons in the conduction band (CB) and the holes in the valence band (VB).

$$E_k^c = \frac{\hbar^2 k^2}{2m_{eff}^c} + E_g$$

$$E_k^v = -\frac{\hbar^2 k^2}{2m_{eff}^v} \tag{9.6}$$

where E_g is the semiconductor bandgap and the energies are relative to the top of the valence band. In this approximation the carriers behave as free particles with an 'effective mass', $m_{eff}^{c,v}$. Graphically, the effective mass accounts for the curvature of the conduction and valence bands at $k = 0$. Physically, the effective mass attempts to incorporate the complicated periodic potential felt by the carrier in the lattice. This approximation allows us to completely ignore the semiconductor atoms in the lattice and treat the electron and hole as 'free particles'.

If the effective mass approximation is combined with a spherical boundary condition then each of the carriers in the quantum dot problem is in the 'particle-in-a-sphere' form (Eqn 9.1). However, this step requires that we treat the quantum dot as a 'bulk' sample. In other words, we assume that the single particle (electron or hole) wavefunction can be written in terms of Bloch functions (Eqn 9.5). This approximation, sometimes called the *envelope function approximation* [8,9], is valid when the dot

diameter is much larger than the lattice constant of the material. To satisfy the boundary condition the single particle (sp) wavefunction is then written as a linear combination of Bloch functions

$$\Psi_{sp}(\mathbf{r}) = \sum_k C_{nk} u_{nk}(\mathbf{r}) \exp(i\mathbf{k}\cdot\mathbf{r}) \tag{9.7}$$

with expansion coefficients, C_{nk}. If we assume that the functions u_{nk} have a weak k dependence then Eqn 9.7 can be rewritten as

$$\Psi_{sp}(\mathbf{r}) = u_{n0}(\mathbf{r}) \sum_k C_{nk} \exp(i\mathbf{k}\cdot\mathbf{r}) = u_{n0}(\mathbf{r}) f_{sp}(\mathbf{r}), \tag{9.8}$$

where $f_{sp}(\mathbf{r})$ is the single particle 'envelope function'. In the tight-binding approximation [or linear combination of atomic orbitals (LCAO) approximation] the periodic function u_{n0} is written as a sum of atomic wavefunctions, φ_n,

$$u_{n0}(\mathbf{r}) \approx \sum_i C_{ni} \varphi_n(\mathbf{r} - \mathbf{r}_i), \tag{9.9}$$

where the sum is over lattice sites and n represents the conduction band or valence band for the electron or hole, respectively. The functions u_{n0} are known from the bulk material and the quantum dot problem is reduced to determining the envelope functions for the single particle wavefunctions, f_{sp}.

As depicted in Fig. 9.3, during quantum dot optical transitions two particles are created, an electron and a hole. If we assume spherically shaped dots with an infinitely high potential barrier at the dot boundary, the envelope functions of these particles are given by the 'particle-in-a-sphere' solutions, Eqn 9.2. The energy of each carrier is then described by Eqn 9.4 with the free particle mass m_0 replaced by $m_{eff}^{c,v}$.

However, in this treatment we completely ignore the Coulombic attraction between the electron and the positively charged hole. In the bulk material this interaction creates bound hydrogenic-like states, or excitons [4]. Since this effect is also present in quantum dots [10], a third approximation, the *strong confinement approximation* [1–3], is used to justify the neglect of this term. According to Eqn 9.4, the confinement energy of each carrier scales as $1/a^2$. The Coulomb interaction scales as $1/a$. In sufficiently small dots the quadratic confinement terms dominates. This condition is satisfied when the size of the quantum dot is much smaller than the size of the bulk exciton. In this strong confinement size regime the electron and hole are treated independently and each is described as a 'particle-in-a-sphere' [1–3]. The Coulomb term may then be added as a first-order energy correction, E_C. Therefore, using Eqns 9.4 and 9.8 the electron–hole pair (ehp) states are written as:

$$\begin{aligned}\Psi_{ehp}(\mathbf{r}_e, \mathbf{r}_h) &= \Psi_e(\mathbf{r}_e)\Psi_h(\mathbf{r}_h) = u_c f_e(\mathbf{r}_e) u_v f_h(\mathbf{r}_h) \\ &= C\left[u_c \frac{j_{L_e}(k_{n_e,L_e} r_e) Y_{L_e}^{m_e}}{r_e}\right]\left[u_v \frac{j_{L_h}(k_{n_h,L_h} r_h) Y_{L_h}^{m_h}}{r_h}\right]\end{aligned} \tag{9.10}$$

with energies

$$E_{ehp}(n_h L_h n_e L_e) = E_g + \frac{\hbar^2}{2a^2}\left\{\frac{\alpha_{n_h,L_h}^2}{m_{eff}^v} + \frac{\alpha_{n_e,L_e}^2}{m_{eff}^c}\right\} - E_C. \tag{9.11}$$

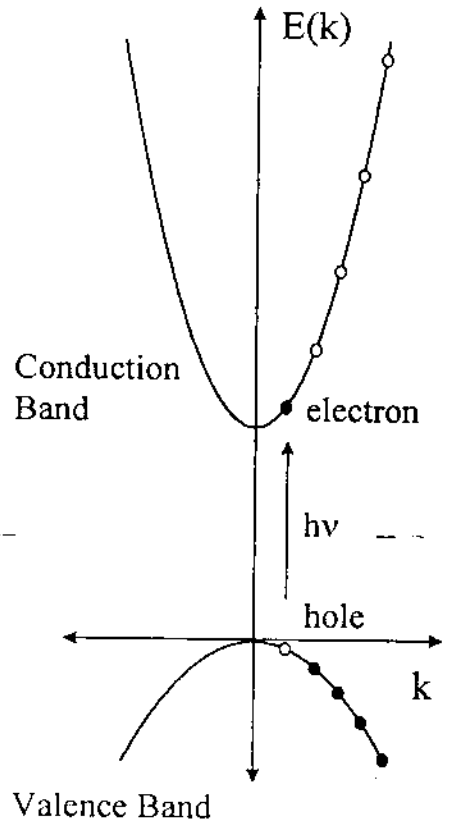

Figure 9.3 Optical transitions in finite size semiconductor quantum dots are discrete due to the quantization of the bulk band diagram. An electron is promoted into the conduction band, creating a hole in the valence band.

The states are labelled by the quantum numbers $n_h L_h n_e L_e$. For example, the lowest pair state is written as $1S_h1S_e$. For pair states with the electron in the $1S_e$ level, the first-order Coulomb correction, E_c, is $1.8e^2/\varepsilon a$, where ε is the dielectric constant of the semiconductor [3]. Equations 9.10 and 9.11 are usually referred to as the 'particle-in-a-sphere' solutions to the quantum dot spectrum.

2.1.2 OPTICAL TRANSITION PROBABILITIES

For a particular quantum dot pair state the transition probability is given by the dipole matrix element

$$P = |\langle \Psi_{ehp} | \mathbf{e} \cdot \hat{p} | 0 \rangle|^2, \tag{9.12}$$

where $|0\rangle$ is the vacuum state, $\mathbf{e}$ is the polarization vector of the light, and $\hat{p}$ is the momentum operator. In the strong confinement approximation where the carriers are treated independently, Eqn 9.12 is commonly rewritten in terms of the single particle states

$$P = |\langle \Psi_e | \mathbf{e} \cdot \hat{p} | \Psi_h \rangle|^2. \tag{9.13}$$

Since the envelope functions are slowly varying in terms of **r**, the operator $\hat{p}$ acts only on the unit cell portion (u_{nk}) of the wavefunction. Equation 9.13 is simplified to

$$P = |\langle u_c|\mathbf{e}\cdot\hat{p}|u_v\rangle|^2|\langle f_e|f_h\rangle|^2. \tag{9.14}$$

In the 'particle-in-a-sphere' model this yields

$$P = |\langle u_c|\mathbf{e}\cdot\hat{p}|u_v\rangle|^2\delta_{n_e,n_h}\delta_{L_e,L_h} \tag{9.15}$$

due to the orthonormality of the 'particle-in-a-sphere' envelope functions. Therefore, simple selection rules ($\Delta n = 0$ and $\Delta L = 0$) are obtained in the 'particle-in-a-sphere' model.

2.1.3 THE REAL BAND STRUCTURE

In the above model the bulk conduction and valence bands are approximated by simple parabolic bands (Fig. 9.2). However, in general the band structure of II–VI semiconductors, such as CdSe, is more complicated. While the conduction band is well approximated by the simple treatment, the valence band is not. The valence band arises from Se 4p atomic orbitals and is 6-fold degenerate at $k = 0$, including spin. (In contrast, the conduction band arises from Cd 5s orbitals and is only 2-fold degenerate at $k = 0$.) When this degeneracy is lifted, valence band substructure occurs. For quantum dot pair states, this structure strongly modifies the results of the 'particle-in-a-sphere' model [11].

For convenience CdSe is often approximated as having the diamond-like band structure illustrated in Fig. 9.4. Due to strong spin–orbit coupling ($\Delta = 0.42$ eV in CdSe [12]) the valence band degeneracy at $k = 0$ is split into $p_{3/2}$ and $p_{1/2}$ sub-bands, where the subscript refers to $J = l + s$ ($l = 1$, $s = 1/2$). Away from $k = 0$ the $p_{3/2}$ band is further split into $J_m = \pm 3/2$ and $J_m = \pm 1/2$ sub-bands. The three sub-bands are referred to as either the heavy hole, light hole, and split-off hole sub-bands, or the A, B, and C sub-bands, as shown in Fig. 9.4.

For CdSe the structure in Fig. 9.4 is an approximation for two reasons.

1 Figure 9.4 ignores the crystal field splitting which occurs in CdSe crystals with a wurtzite (or hexagonal) lattice. This lattice, with its unique 'c' axis, has a crystal field which lifts the degeneracy of the A and B bands at $k = 0$ as shown in Fig. 9.5. This 'A–B splitting' is small (25 meV [10]) in bulk CdSe and is often neglected in quantum dot calculations. However, we discuss below how this term can cause additional splittings in the quantum dot transitions.

2 While the diamond structure has inversion symmetry, the hexagonal CdSe lattice does not. In detailed calculations this lack of inversion symmetry leads to linear terms in k which further split the A and B sub-bands in Fig. 9.5 away from $k = 0$ [13]. Since these linear terms are extremely small, they are generally neglected and are ignored below.

2.1.4 THE $k\cdot p$ METHOD (PRONOUNCED K-DOT-P)

Due to the complexity of the real band structure accurate quantum dot calculations require one to go beyond the 'particle-in-a-sphere' model and incorporate a better

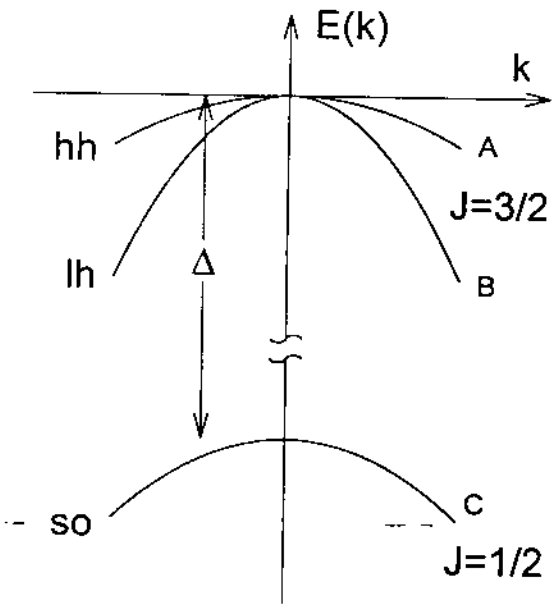

Figure 9.4 Simplified illustration of valence band structure at $k = 0$ for diamond-like semiconductors. Due to spin–orbit coupling (Δ) the valence band is split into two bands ($J = 3/2$ and $J = 1/2$) at $k = 0$. Away from $k = 0$, the $J = 3/2$ band is further split into the $J_m = \pm 3/2$ heavy hole (hh or A) and the $J_m = \pm 1/2$ light hole (lh or B) sub-bands. The $J = 1/2$ band is referred to as the split-off (so or C) band.

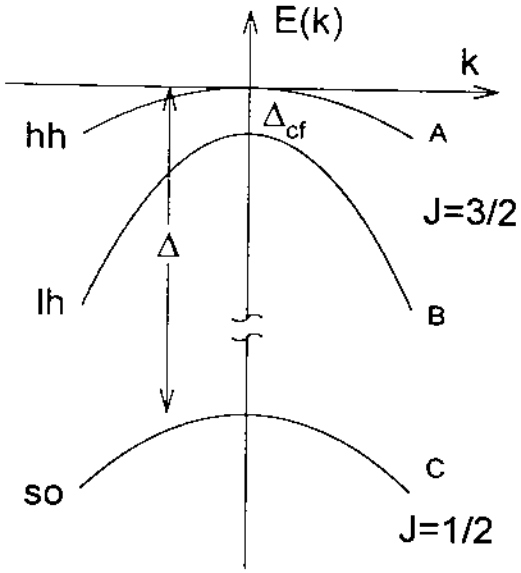

Figure 9.5 Simplified illustration of the bulk valence band for wurtzite (hexagonal) CdSe near $k = 0$. Due to the crystal field of the hexagonal lattice the A and B bands are split by Δ_{cf} (25 meV) at $k = 0$.

description of the bulk bands. Although bulk band structure can be determined with high accuracy using a variety of computational methods, these methods rarely provide analytical expressions for the description of the bands. For this purpose a much simpler, but often sufficient approach, the $k \cdot p$ method, is used [14]. In this method the bulk bands are expanded analytically around a particular point in k-space, typically $k = 0$.

Around this point the band energies and wavefunctions are then expressed in terms of the periodic functions u_{nk} and their energies E_{nk}.

To derive general expressions for u_{nk} and E_{nk} within this approach one considers the Bloch functions in Eqn 9.5. These functions are solutions of the Schrödinger equation for the single particle Hamiltonian

$$H_0 = \frac{p^2}{2m_0} + V(x), \tag{9.16}$$

where $V(x)$ is the periodic potential of the crystal lattice. Using Eqns 9.5 and 9.16 it is simple to show that the periodic functions, u_{nk}, satisfy the equation

$$\left[H_0 + \frac{1}{m_0}(k \cdot p)\right] u_{nk} = \lambda_{nk} u_{nk}, \tag{9.17}$$

where

$$\lambda_{nk} = E_{nk} - \frac{k^2}{2m_0}. \tag{9.18}$$

Since u_{n0} and E_{n0} are assumed known, Eqn 9.17 can be treated in perturbation theory around $k = 0$ with

$$H' = \frac{(k \cdot p)}{m_0}. \tag{9.19}$$

Then using non-degenerate perturbation theory to second order* one obtains the energies

$$E_{nk} = E_{n0} + \frac{k^2}{2m_0} + \frac{1}{m_0^2} \sum_{m \neq n} \frac{|\mathbf{k} \cdot \mathbf{p}_{nm}|^2}{E_{n0} - E_{m0}} \tag{9.20}$$

and functions

$$u_{nk} = u_{n0} + \frac{1}{m_0} \sum_{m \neq n} u_{m0} \frac{\mathbf{k} \cdot \mathbf{p}_{mn}}{E_{n0} - E_{m0}} \tag{9.21}$$

with

$$\mathbf{p}_{nm} = \langle u_{n0} | \mathbf{p} | u_{m0} \rangle. \tag{9.22}$$

The summations in Eqns 9.20 and 9.21 are over all bands $m \neq n$. As one might expect the dispersion of band n is due to coupling with nearby bands.

Therefore, with the $k \cdot p$ approach analytical expressions can be obtained which describe the bulk bands to second order in k. While our discussion here outlines the general method, the approach must be slightly modified for CdSe. First, for the CdSe valence band, degenerate perturbation theory must be used. In this case the valence band must be diagonalized before coupling with other bands is considered. Second, we

*Inversion symmetry is assumed. In CdSe the lack of inversion symmetry introduces terms linear in k. These terms are small and generally neglected.

have neglected spin–orbit coupling terms. However, these terms are easily added as can be seen in Kittel [14].

2.1.5 THE KANE MODEL

In some bulk systems it is necessary to go beyond second order in the $k \cdot p$ approach to properly describe the bands. However, in higher orders this approach is often cumbersome and Kane [15,16] developed an alternate procedure for bulk semiconductors which is also widely used in confined systems. In the Kane model a small subset of bands are treated exactly by explicitly diagonalizing Eqn 9.17 (or the equivalent expression with the spin–orbit interaction included). This subset usually contains the bands of interest, e.g. the valence band and conduction band. Then the influence of outlying bands is included within the second-order $k \cdot p$ approach. Due to the exact treatment of the bands of interest, the dispersion of each band is no longer strictly quadratic as in Eqn 9.20. Therefore, the Kane model better describes band 'non-parabolicities'.

2.1.6 THE LUTTINGER HAMILTONIAN

For bulk diamond-like semiconductors the 6-fold degenerate valence band is described by the Luttinger Hamiltonian [17,18]. This expression, a 6 by 6 matrix, is derived within the context of degenerate $k \cdot p$ perturbation theory [19]. The Hamiltonian is commonly simplified further using the spherical approximation [20–22]. In this case only terms of spherical symmetry in the Luttinger Hamiltonian are considered. 'Warping' terms of cubic symmetry are neglected and, if desired, treated as a perturbation. For quantum dot theories which include the valence band degeneracies, the Luttinger Hamiltonian is the initial starting point to obtain the hole eigenstates and their energies. We note that since CdSe is wurtzite, as discussed above, use of the Luttinger Hamiltonian for CdSe quantum dots is an approximation. It does not include the crystal field splitting that is present in wurtzite CdSe.

2.2 *Experimental*

2.2.1 SAMPLES

Although we focus here on quantum dot spectroscopy, we cannot overemphasize the importance of sample quality in obtaining useful optical information. Fortunately, tremendous progress has been made in recent years in the fabrication of II–VI quantum dots. In particular, extremely high quality CdSe dots can now be prepared according to the method of Murray *et al.* [5], or variations thereof [23]. This procedure uses a wet chemical (organometallic) synthesis to fabricate the crystallites. The size distribution is then further narrowed by a size-selective precipitation step. Highly crystalline, nearly monodisperse (<4% r.m.s.) dots are obtained with well-passivated surfaces. Without further modification these dots exhibit strong band edge luminescence with a quantum yield greater than 0.1 and measured as high as 0.9 at 10 K. At room temperature the

quantum yield is typically 10% [5]. The intensity of 'deep trap' emission,* which dominates the luminescence behaviour of dots prepared by many other methods, is very weak in these samples.

Due to their versatile surface chemistry, the dots can be dispersed in a variety of host materials, such as solvents, polymers, and other semiconductors. In fact, very recently Guyot-Sionnest [24] has reported that CdSe quantum dots encapsulated in a higher band gap semiconductor such as ZnS exhibit room temperature emission quantum yields greater than 0.5. This development, along with the recent demonstrations of both disordered CdSe quantum dot glasses [25] and three-dimensionally ordered CdSe quantum dot arrays [26] are providing exciting new classes of quantum dot materials for future study.

With the synthetic method of Murray *et al.* [5] high quality samples ranging from ~15 Å to ~120 Å in mean diameter are easily produced. Therefore, with such samples one of the original and basic experimental questions about quantum dots — how their electronic spectra evolve with size in the strong confinement regime — may be addressed. Early work on this question [27–34] was constrained by difficulties in preparing high quality, monodisperse samples. Inhomogeneities such as distributions in size and shape which conceal the higher transitions prevented a more complete investigation. More recent studies [35–38] which do examine quantum dots of sufficient quality to resolve many of the higher states are restricted to one [35–37] or a few [38] sizes. The newer samples allow the size dependence question to be more satisfactorily addressed. In addition, their spectra exhibit fine structure in the lowest exciton feature which has been crucial to explaining the luminescence behaviour of these materials [39–41].

2.2.2 SPECTROSCOPIC METHODS

Despite the high quality of these samples, residual sample inhomogeneities still remain which broaden absorption and emission features and conceal transitions. To reduce these effects several spectroscopic techniques may be used. For absorption information the most common technique has been transient differential absorption spectroscopy (TDA), also called pump-probe or hole-burning spectroscopy [35,39,42–53]. This technique measures the absorption change induced by a spectrally narrow pump beam. TDA effectively increases the resolution of the spectrum by optically exciting and bleaching a narrow subset of the quantum dots. The bleach spectrum reveals absorption information with inhomogeneous broadening greatly reduced. However, pump-induced absorption features which overlap with the bleach features of interest complicate the analysis. More recently, many groups have begun to utilize a simpler optical technique which avoids this problem, photoluminescence excitation (PLE) [35,54–57]. Like TDA, PLE selects a narrow subset of the sample distribution and absorption informa-

*'Deep trap' emission is luminescence which is strongly red-shifted from the HOMO–LUMO transition (or 'band edge' in solid-state terminology) of the quantum dot. While the true origin of this luminescence is unknown, it is generally assumed that its presence indicates defect and/or impurity states which are deep in the gap.

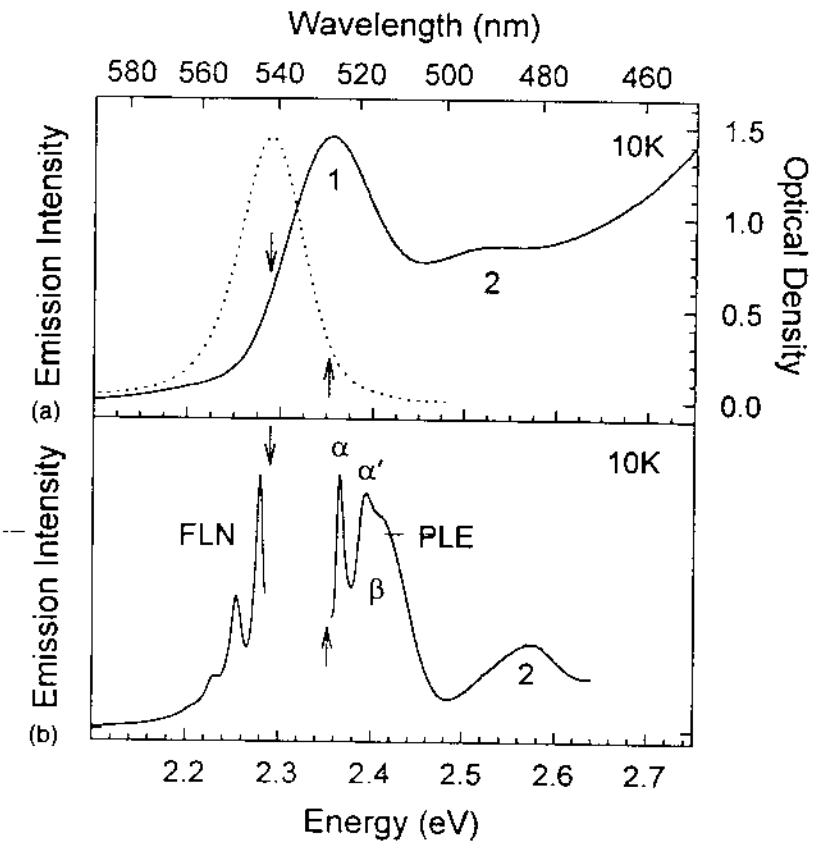

Figure 9.6 (a) Absorption (solid line) and full luminescence (dotted line) spectra for ~19 Å effective radius CdSe quantum dots. (b) Fluorescence line narrowing (FLN) and photoluminescence excitation (PLE) spectra for the same sample. An LO-phonon progression is observed in FLN. Both narrow (α, α') and broad (β) absorption features are resolved in PLE. The downward (upward) arrows denote the excitation (emission) position used for FLN (PLE). (Adapted from [41].)

tion with increased resolution is obtained. When PLE is combined with fluorescence line narrowing (FLN) spectroscopy, both absorption and emission information representative of a 'single dot' is revealed.

Both PLE and FLN techniques are demonstrated in Fig. 9.6 along with absorption and emission results for a 19 Å effective radius CdSe quantum dot sample.* On this scale only the lowest two exciton features are observed in the absorption spectrum (solid line in Fig. 9.6a). The emission spectrum (dotted line in Fig. 9.6a) is obtained by exciting the sample well above its first transition so that emission occurs from the entire sample distribution. This inhomogeneously broadened emission feature is referred to as 'full luminescence'. If instead a subset of the sample distribution is excited, a significantly narrowed and structured emission spectrum is revealed. For example, when the sample in Fig. 9.6 is excited on the low energy side of its first absorption feature (downward arrows in Fig. 9.6) a vibration (longitudinal optical (LO) phonon) progres-

*Sizes reported are estimated from extensive size-dependent transmission electron microscopy (TEM) and small angle X-ray measurements and are based on the energy of the first absorption peak. We define the effective radius of our prolate dots as $a = [(b^2c)^{1/3}]/2$ where b and c are the short and long axes, respectively.

sion is clearly resolved. This FLN spectrum can be used to extract a model 'single dot' emission lineshape.

PLE can similarly be used to extract 'single dot' absorption information by monitoring a narrow spectral band (upward arrows) of the full luminescence while scanning the excitation energy. As seen in Fig. 9.6(b), both absorption features present in Fig. 9.6(a) are obtained with higher resolution. In addition structure is observed with the lowest absorption feature. As we show below these features (α and β) represent fine structure present in the lowest exciton and have important implications for quantum dot emission. However, before discussing the exciton fine structure, in the next section we use PLE results on a large series of CdSe samples to describe the size dependence of the exciton structure.

2.3 *Exciton structure vs size*

2.3.1 EXPERIMENTAL RESULTS

While the absorption and PLE spectra in Fig. 9.6 show only the two lowest exciton features, current samples reveal much more exciton structure. For example, in Fig. 9.7 PLE results for a 28 Å radius CdSe sample are shown along with its absorption and full luminescence spectra. These data cover a larger spectral range than Fig. 9.6 and show more of the exciton spectrum. To determine how the exciton structure evolves with quantum dot size, PLE data can be obtained for a large sample series. Seven such spectra are shown in Fig. 9.8. The quantum dots are arranged (top to bottom) in order of increasing radius from ~15 to ~43 Å. Quantum confinement clearly shifts the transitions blue (>0.5 eV) with decreasing size. The high quality of these dots also allows the resolution of as many as eight absorption features in a single spectrum.

By extracting peak positions from PLE data such as Fig. 9.8 the quantum dot spectrum as a function of size is obtained. Figure 9.9 plots the final size-dependent spectrum determined in [57]. Although dot radius (or diameter) is not used as the x-axis, Fig. 9.9 still represents a 'size-dependent' plot. The x-axis label, the energy of the first excited state, is a strongly size-dependent parameter. It is also much easier to measure accurately than quantum dot size. For the y-axis the energy relative to the first excited state is used so that the plot focuses on the higher excited states. Therefore, Fig. 9.9 summarizes the size dependence of the first 10 transitions for CdSe quantum dots in the strong confinement regime.

2.3.2 COMPARISON WITH THEORY

In order to understand this result one could begin with the simple 'particle-in-a-sphere' model outlined above (see Section 2.1.1). The complicated valence band structure, shown in Fig. 9.4, could then be included by considering each sub-band (A, B, and C) as a simple parabolic band. In such a zero-order picture each bulk sub-band would lead to a ladder of 'particle-in-a-sphere' states for the hole, as shown in Fig. 9.10. Quantum dot transitions would occur between these hole states and the electron levels arising from the bulk conduction band. However, we find that this simplistic approach fails to describe the experimental absorption structure. In particular two avoided crossings are

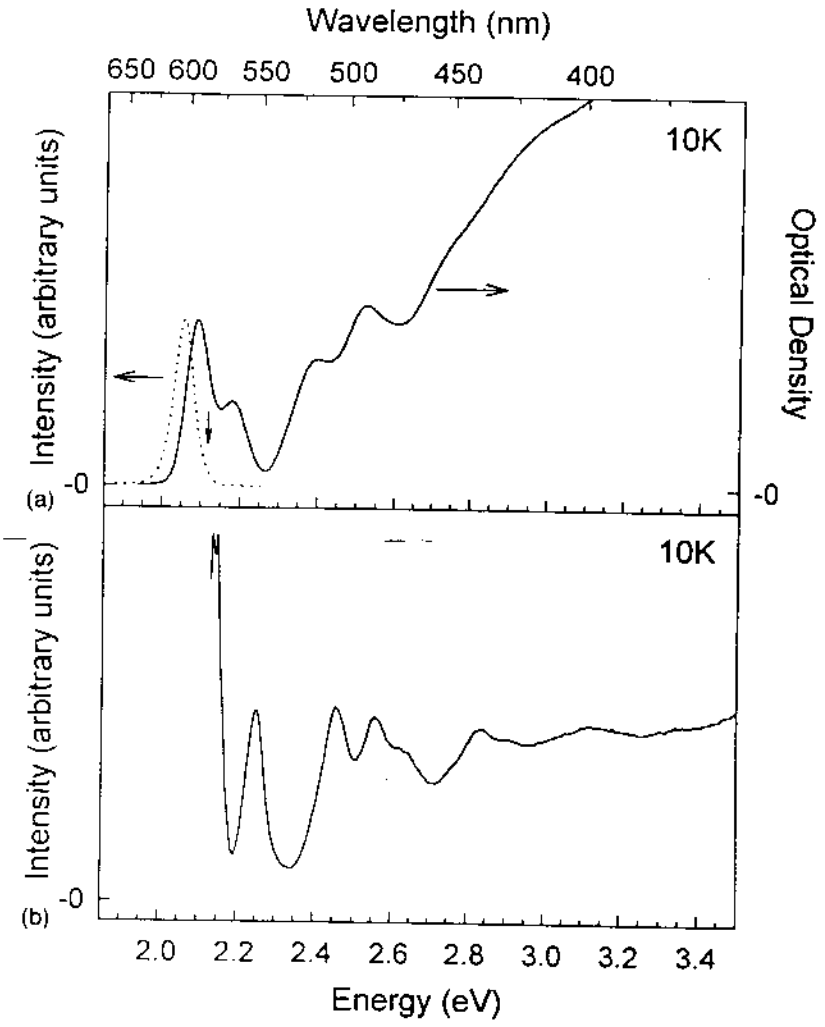

Figure 9.7 (a) Absorption (solid line) and full luminescence (dashed line) spectra for ~28 Å radius CdSe quantum dots. In luminescence the sample was excited at 2.655 eV (467.0 nm). The downward arrow marks the emission position used in photoluminescence excitation (PLE). (b) PLE scan for the same sample. (Adapted from [57].)

present in Fig. 9.8 (between features (e) and (g) at ~2.0 eV and between features (e) and (c) above 2.2 eV) and these are not predicted by this 'particle-in-a-sphere' model.

The problem lies in the assumption that each valence sub-band produces its own independent ladder of hole states. In reality the hole states are mixed due to the underlying quantum mechanics. To help understand this effect, we summarize all of the relevant quantum numbers in Fig. 9.11. The total angular momentum of either the electron or hole (F_e or F_h) has two contributions (i) a 'unit cell' contribution (J) due to the underlying basis which forms the bulk bands; and (ii) an envelope function contribution (L) due to the 'particle-in-a-sphere' orbital. Above we assume that the quantum numbers describing each valence sub-band (J_h) and each envelope function (L_h) are conserved. However, when the Luttinger Hamiltonian, which describes the bulk valence band, is combined with a spherical potential, mixing between the bulk valence bands occurs. This effect, which was first shown for bulk impurity centres [20–22], also mixes quantum dot hole states [11,38,58–61]. Only parity and the total

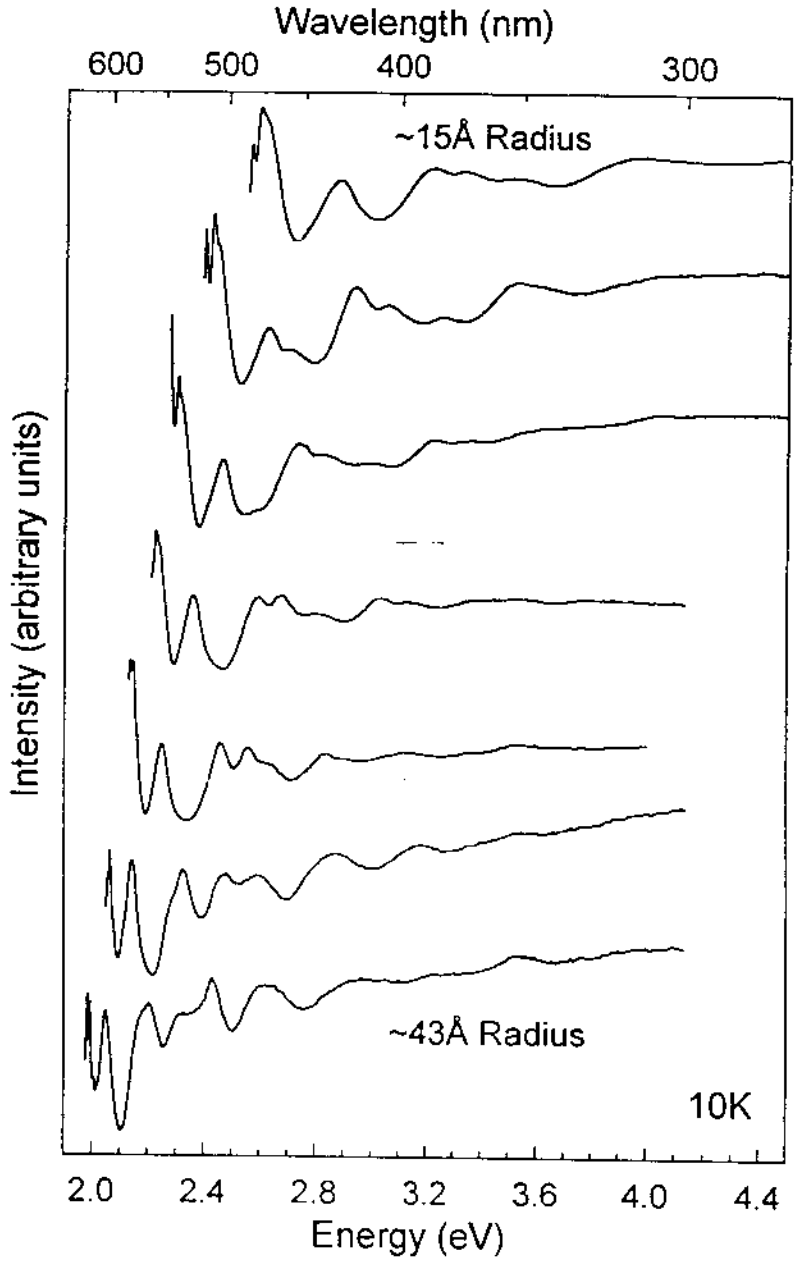

Figure 9.8 Normalized photoluminescence excitation (PLE) scans for seven different size quantum dot samples. Size increases from top to bottom and ranges from ~15 to ~43 Å in radius. (Adapted from [57].)

hole angular momentum (F_h) are good quantum numbers. Neither L_h nor J_h are conserved. Therefore, each quantum dot hole state is a mixture of the three valence sub-bands (valence band mixing) as well as 'particle-in-a-sphere' envelope functions with angular momentum L_h and $L_h + 2$ ('S–D mixing'). The three independent ladders of hole states shown in Fig. 9.10 are coupled. The electron levels which originate in the simple conduction band are not affected by the valence band complexities and are well described by the 'particle-in-a-sphere' ladder.

When these effects are included theory correctly describes the observed size-

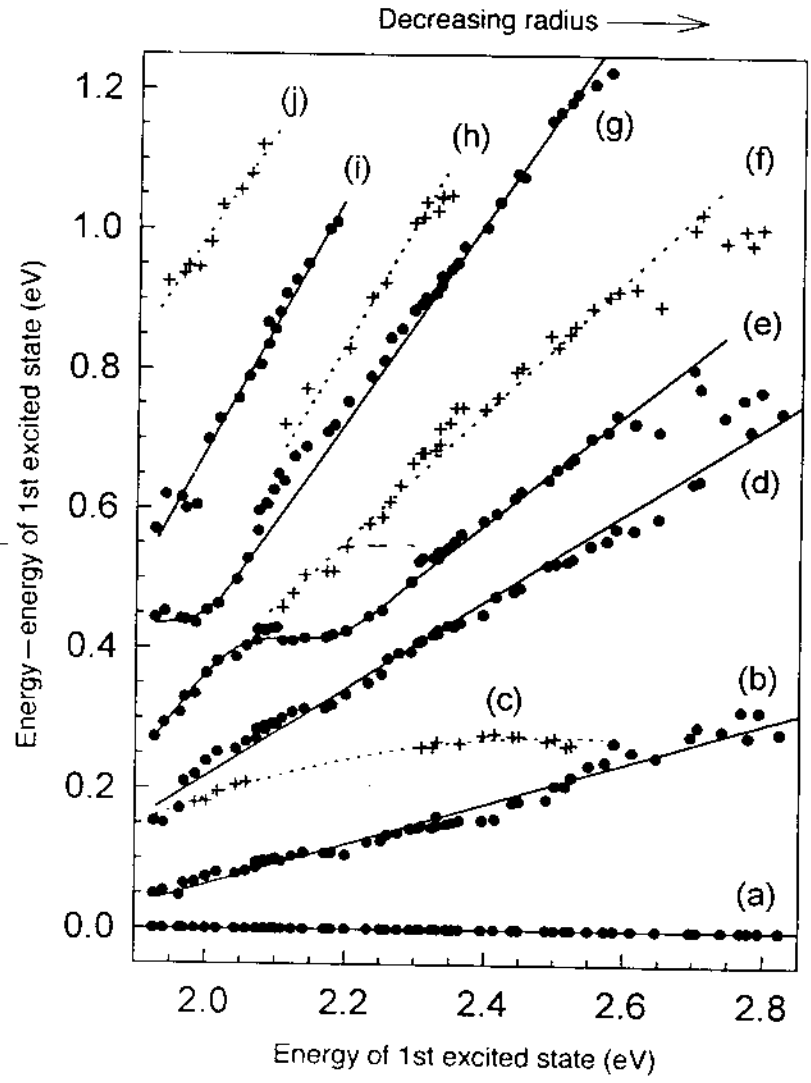

Figure 9.9 Transition energies (relative to the first excited state) vs the energy of the first excited state. Peak positions are extracted from photoluminescence excitation (PLE) data such as that shown in Fig. 9.8. Strong (weak) transitions are denoted by circles (crosses). The solid (dashed) lines are visual guides for the strong (weak) transitions to clarify their size evolution. (Adapted from [57].)

dependent absorption structure. Using the approach of Efros [38,58] in which the energies of the hole states are determined by solving the Luttinger Hamiltonian and the electron levels are calculated within the Kane model, strong agreement with the data is obtained, as shown in Figs 9.12 and 9.13. Figure 9.12 compares theory with the lowest three transitions which exhibit simple size-dependent behaviour (i.e. no avoided crossings). Figure 9.13 shows the avoided crossing regions. The transitions can be assigned and labelled by modified 'particle-in-a-sphere' symbols which account for the valence band mixing discussed above [57].

Although theory clearly predicts the observed avoided crossings, Fig. 9.13 also demonstrates that theory underestimates the repulsion in both avoided crossing regions, causing theoretical deviation in the predictions of the $1S_{1/2}1S_e$ and $2S_{1/2}1S_e$

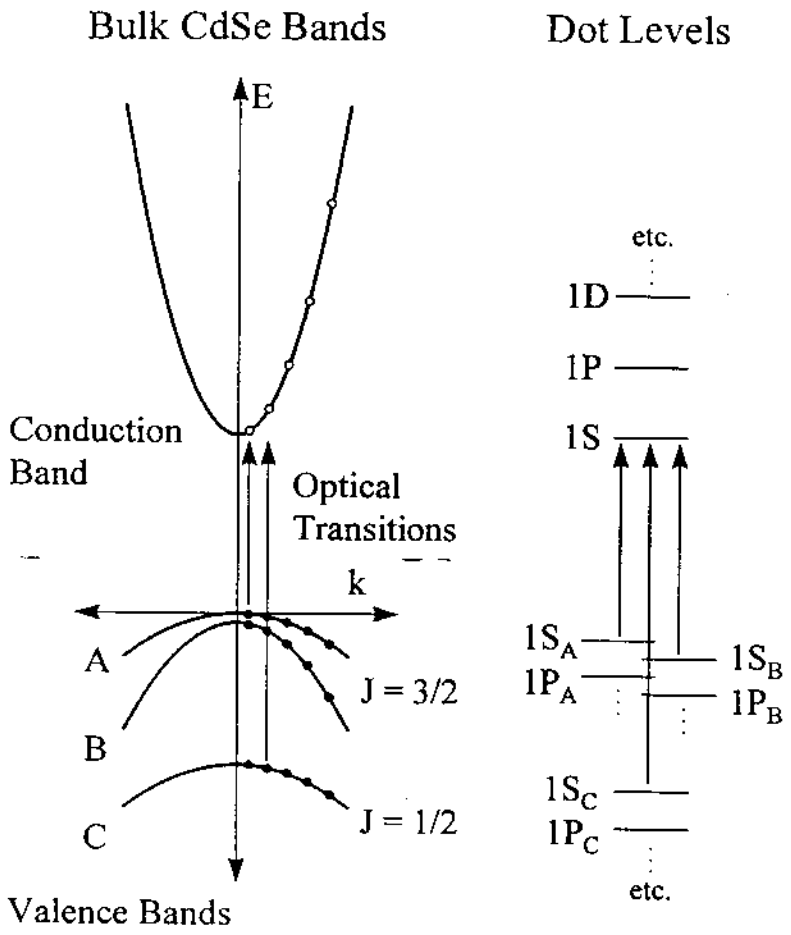

Figure 9.10 A simplistic approach to describing the quantum dot spectrum. If we consider each valence sub-band independently, each contributes a ladder of 'particle-in-a-sphere' states for the hole. The transitions then occur between these hole states and the electron levels arising from the conduction band. However, this zero-order model fails to predict the observed structure due to mixing of the different hole ladders, as discussed in the text.

transitions. This discrepancy is most likely due to the Coulomb mixing of the electron–hole pair states, which is ignored by the model (via the strong confinement approximation). If included this term would further couple the $nS_{1/2}1S_e$ transitions such that these states 'push off' each other more strongly. In addition the Coulomb term would cause the $1S_{1/2}1S_e$ and $2S_{1/2}1S_e$ states to avoid one another through their individual repulsion from the strongly allowed $1P_{3/2}1P_e$. A current area of theoretical research is to include a more rigorous treatment of the Coulomb mixing and correct these discrepancies.

Despite these discrepancies, however, theory is clearly on the right track. Therefore, since the transitions are now assigned, we can use the model to understand the physics behind the avoided crossings. As discussed above, in the zero-order picture of Fig. 9.10 each valence sub-band contributes a ladder of hole states. Due to spin–orbit splitting (see Fig. 9.5) the C band ladder is offset 0.42 eV below the A and B band ladders. This leads to possible resonances between hole levels from the A and B bands with C band levels. Since the levels are spreading out with decreasing dot size, resonance conditions are satisfied only in certain size dots. Figure 9.14 demonstrates the two resonances responsible for the observed avoided crossings. For simplicity we treat the A and B

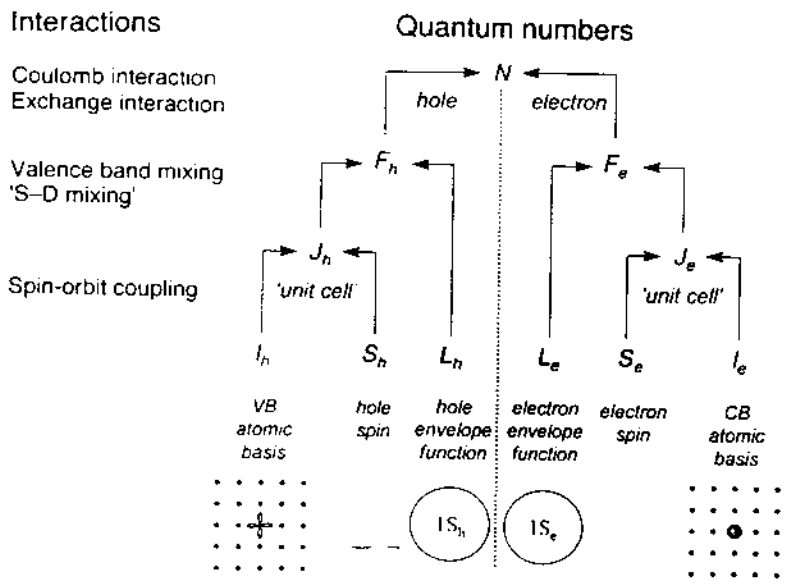

Figure 9.11 Summary of quantum dot quantum numbers and important interactions. The total electron–hole pair angular momentum (N) has contributions due to both the electron (F_e) and hole (F_h). Each carrier's angular momentum (F) may then be further broken down into a 'unit cell' component (J) due to the atomic basis (I) and spin (s) of the particle and an envelope function component (L) due to the 'particle-in-a-sphere' orbital.

bands together. For example, in Fig. 9.14(a) the $2D$ level from the A and B bands is resonant with the 1S level from the C band. The size dependence of these levels is plotted in Fig. 9.14(c). Due to both valence band mixing and S–D mixing, these resonant conditions lead to the observed avoided crossings. Although this description is based on the simple 'particle-in-a-sphere' model of Fig. 9.10, the explanation is consistent with a more detailed analysis [57].

2.4 *Exciton fine structure*

2.4.1 PERTURBATIONS TO THE SPHERICAL MODEL

In the previous section, we have shown that the exciton structure of CdSe quantum dots is now fairly well understood. In general the size-dependent absorption features are described by quantum dot effective mass models which incorporate the complexities of the CdSe valence band. For convenience these models assume spherical dots and work within the spherical band approximation [20–22], since more sophisticated treatments have not been required to explain experimental results. These models predict that the lowest energy electron–hole pair state ($1S_{3/2}1S_e$ — which we refer to as the 'band edge exciton') is 8-fold degenerate. However, recent theoretical work which extends the 'spherical model' to include the effects of the hexagonal lattice [62], the non-spherical shape [63], and the electron–hole exchange interaction [64–66] has predicted that exciton fine structure should be present. In this case the initially 8-fold degenerate band edge exciton is split into five sublevels [40].

This exciton fine structure is shown in the energy level diagram of Fig. 9.15. To

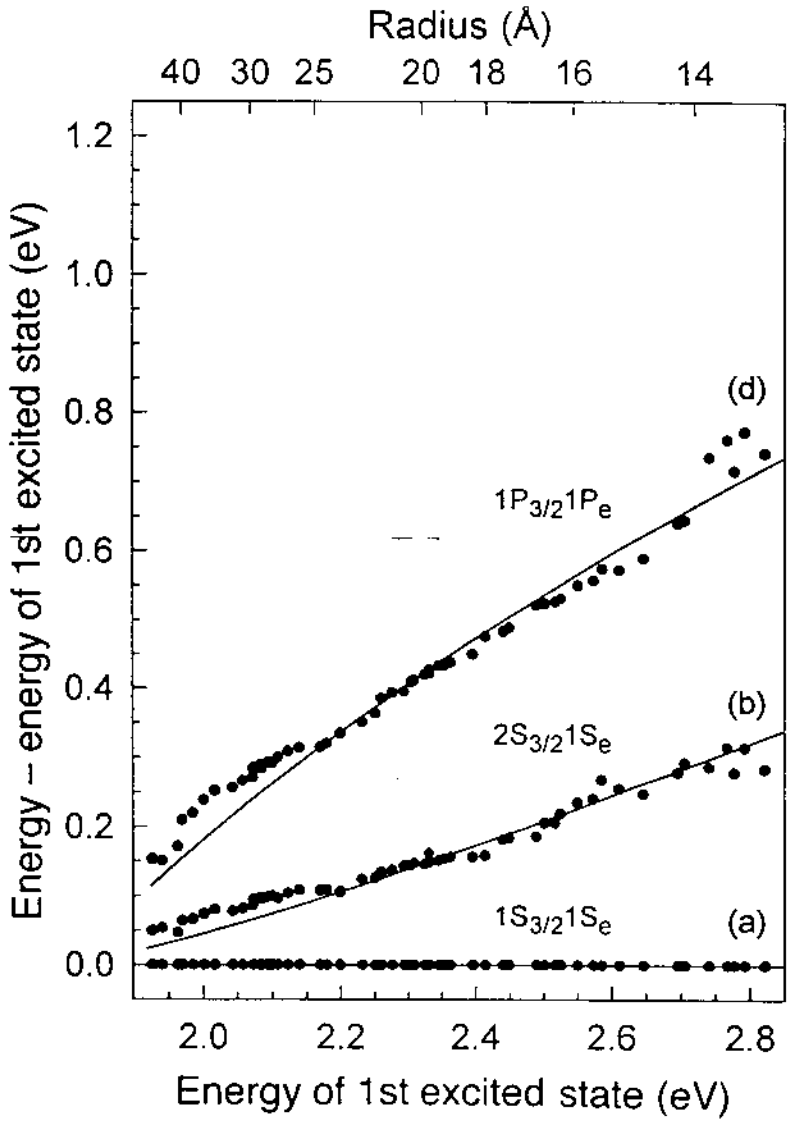

Figure 9.12 Theoretically predicted pair states (solid lines) assigned to features (a), (b), and (d) in Fig. 9.9. The experimental data is shown for comparison (circles). (Adapted from [57].)

describe the structure we consider two limits. On the left of Fig. 9.15 the effect of the anisotropy of the crystal lattice and/or the non-spherical shape of the crystallite dominates. This corresponds to the bulk limit where the exchange interaction between the electron and hole is negligible (0.15 meV [67]). The band edge exciton is split into two 4-fold degenerate states, analogous to the bulk 'A–B splitting' (see Fig. 9.5). The splitting occurs due to the reduction from spherical to uniaxial symmetry. However, since the exchange interaction is proportional to the overlap between the electron and hole, in small dots this term is strongly enhanced due to the confinement of the carriers [64]. Therefore, the right of Fig. 9.15 represents the 'small dot' limit where the exchange interaction dominates. In this case the important quantum number is the total angular momentum, N (see Fig. 9.11). Since $F_h = 3/2$, and $F_e = 1/2$, the band edge exciton is split into a 5-fold degenerate $N = 2$ state and a 3-fold degenerate $N = 1$ state. In the middle of Fig. 9.15 the correlation diagram between these two limits is shown.

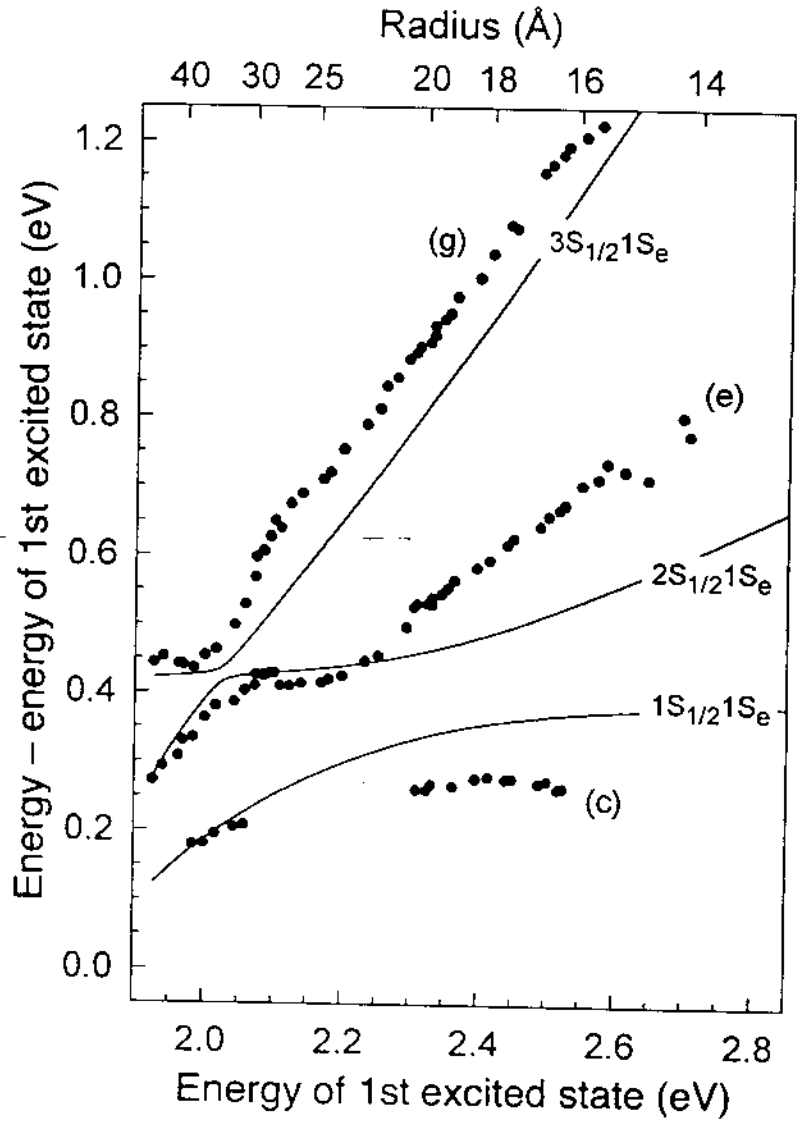

Figure 9.13 Theoretically predicted pair states (solid lines) assigned to features (c), (e), and (g) in Fig. 9.9. The experimental data are shown for comparison (circles). (Adapted from [57].)

When both effects are included, the good quantum number is the projection of N along the unique crystal axis, N_m. The five sublevels are then labelled by $|N_m|$: one sublevel with $|N_m| = 2$, two with $|N_m| = 1$, and two with $|N_m| = 0$. Levels with $|N_m| > 0$ are 2-fold degenerate.

To quantify these effects, the anisotropy and exchange terms can be added to the spherical model within the framework of perturbation theory [40]. Figure 9.16 shows the calculated size dependence of the exciton fine structure. The five sublevels are labelled by $|N_m|$ with superscripts to distinguish upper (U) and lower (L) sublevels with the same $|N_m|$. Their energy, relative to the 1^L sublevel, is plotted vs effective radius. The enhancement of the exchange interaction with decreasing dot size is clearly present.

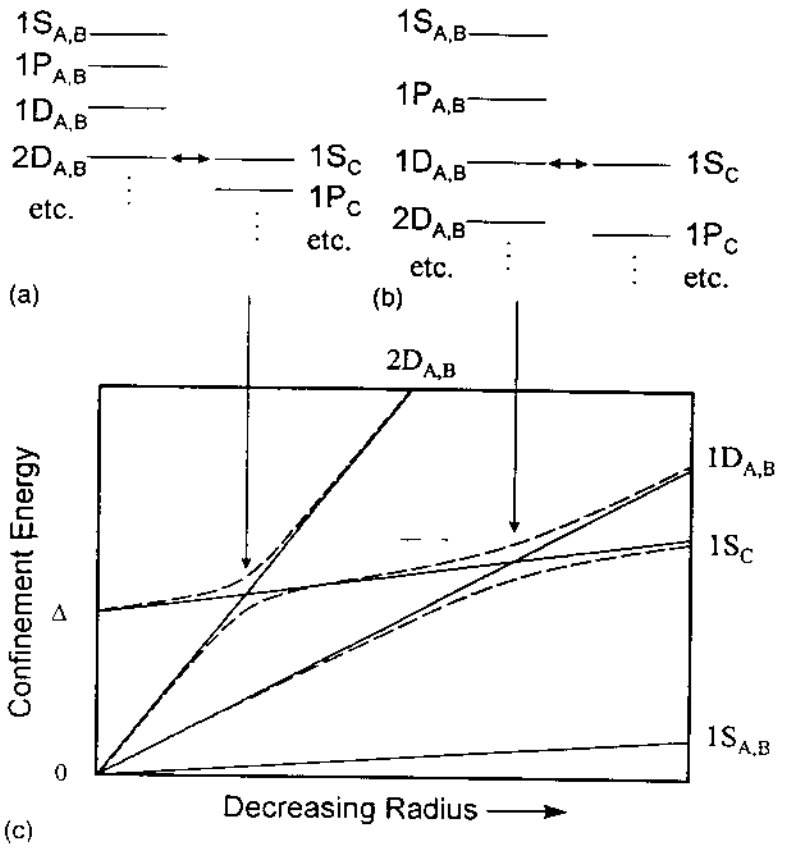

Figure 9.14 Origin of the observed avoided crossings. For a particular quantum dot size a resonance occurs between a hole level from the A and B bands (combined for simplicity) and a hole level from the C band. Energy level diagrams for the hole states are shown in (a) and (b) for the two resonances responsible for the observed avoided crossings. (c) The energy of the hole states vs decreasing radius. The solid (dashed) lines represent the levels without (with) the valence band and S–D mixing.

2.4.2 IMPLICATIONS OF EXCITON FINE STRUCTURE: THE 'DARK EXCITON'

While exciton recombination in bulk II–VI semiconductors occurs with a ~1 ns lifetime [68], CdSe quantum dots exhibit a ~1 μs radiative lifetime at 10 K. This effect is perhaps not surprising in early samples which were of poor quality and emitted weakly via 'deep trap' fluorescence. However, more recent samples which are of much higher quality and emit strongly at the band edge also have long radiative lifetimes [40,69,70]. To explain this behaviour, quantum dot emission has been rationalized by many researchers (including the authors) as a 'surface effect' [35,69–73]. The anomalous emission lifetime has been explained by localization of the photoexcited electron [71–73] and/or hole [35,69,70] at the dot/matrix interface. Once the carriers are localized in surface 'traps', the decrease in carrier overlap increases the recombination time. The influence of the surface on quantum dot emission was considered reasonable since these materials have such large surface-to-volume ratios (e.g. in a ~30 Å diameter dot ca one-third of the atoms are on the surface). This 'surface model' can explain the

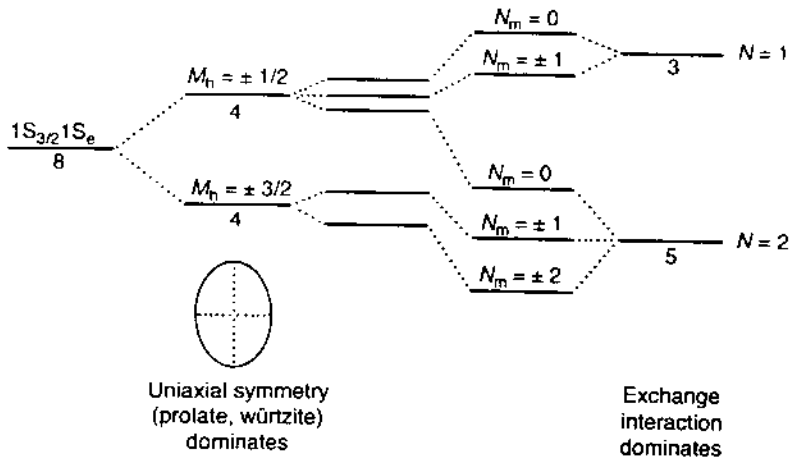

Figure 9.15 Energy level diagram describing the exciton fine structure. In the spherical model the band edge exciton ($1S_{3/2}1S_e$) is 8-fold degenerate. This degeneracy is split by the non-spherical shape of the dots, their hexagonal (wurtzite) lattice, and the exchange interaction. On the left of the diagram, the effects of the non-spherical shape and hexagonal lattice dominate and the band edge exciton is split into two 4-fold degenerate states. This corresponds to the bulk limit. On the right, the exchange interaction dominates and the band edge exciton is split into a 5-fold degenerate $N = 2$ state and a 3-fold degenerate $N = 1$ state. This corresponds to the 'small dot' limit. The middle represents a correlation diagram between these two extremes.

long radiative lifetimes, luminescence polarization results [70], and even the unexpectedly high longitudinal optical (LO) phonon coupling observed in emission [69].

However, the presence of band edge exciton fine structure provides an alternative explanation for the anomalous emission behaviour [40,66,74]. Emission from the lowest band edge state, $|N_m| = 2$, is optically forbidden in the electric dipole approxi-

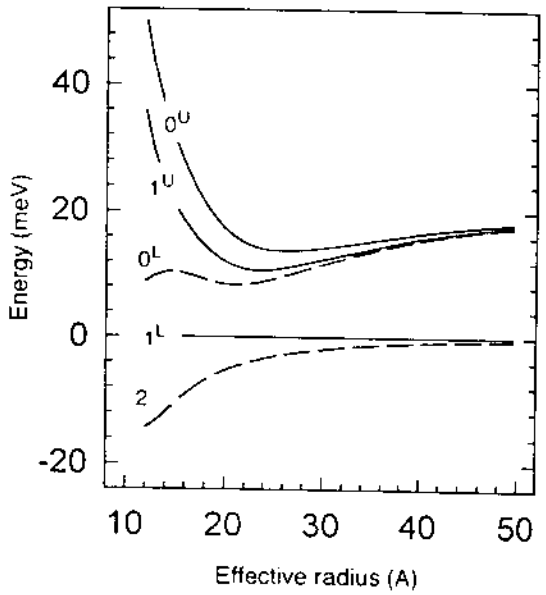

Figure 9.16 Calculated band edge exciton ($1S_{3/2}1S_e$) structure vs effective radius. The sublevels are labelled by $|N_m|$ with superscripts to distinguish upper (U) and lower (L) sublevels with the same $|N_m|$. Positions are relative to 1^L. Optically active (passive) levels are shown as solid (dashed) lines. (Adapted from [41].)

mation. Relaxation of the electron–hole pair into this state, referred to as the 'dark exciton', can explain the long radiative lifetimes observed in CdSe quantum dots, previously attributed to surface traps. Since two units of angular momentum are required to return to the ground state from the $|N_m| = 2$ sublevel, this transition is one-photon forbidden. However, less efficient, phonon-assisted transitions can occur, explaining the stronger LO–phonon coupling of the emitting state and the long radiative lifetimes (at 10 K). In addition polarization effects observed in luminescence [70] can be rationalized by relaxation from the 1^L sublevel to the dark exciton, as shown by Chamarro *et al.* [66].

2.4.3 SPECTROSCOPIC EVIDENCE FOR EXCITON FINE STRUCTURE

We mentioned in Section 2.2.2 that the PLE spectra of high quality samples exhibit additional absorption structure within the lowest exciton feature. For example, in Fig. 9.6(b) a narrow feature (α), its LO phonon replica (α′), and a broader feature (β) are observed. To test whether this structure is consistent with the predicted fine structure, a size-dependent study is shown in Fig. 9.17. For eight different size CdSe samples the band edge FLN/PLE structure is measured. In each FLN/PLE pair the FLN excitation and PLE emission energies are the same and the data are plotted relative to this energy. The actual excitation/emission positions are indicated with arrows in the full luminescence spectra, shown in Fig. 9.18. From the experimental data an underlying lineshape can be extracted for each sample [41]. The single dot lineshape obtained for the sample from Fig. 9.6 is shown in Fig. 9.19. To be consistent with the exciton fine structure the emitting state must be assigned to the dark exciton. The narrow absorption feature (α) is then assigned to the 1^L sublevel since the 0^L sublevel is optically passive. The broader feature (β) is assigned to a combination of the 1^U and the 0^U sublevels.

The assignment of β to a combination of 1^U and 0^U is further supported by data from the larger samples in which a third absorption feature is observed. In Fig. 9.20 the band edge region of FLN/PLE data for a ~44 Å effective radius sample is shown. While in Fig. 9.6(b) three band edge states are resolved — a narrow emitting state, a narrow absorbing state (α), and a broad absorbing state (β) — in Fig. 9.20 four band edge states are present — a narrow emitting state and three narrow absorbing states (α, β_1 and β_2) [41]. In this case β_1 and β_2 can be assigned to the individual 1^U and 0^U sublevels.

To quantitatively test these assignments we compare the experimental results with the predictions of theory in Fig. 9.21. Figure 9.21(a) shows the size dependence of the calculated band edge structure. Figure 9.21(b) shows the position of the absorbing (filled circles and squares) and emitting (open circles) features from Fig. 9.17 and TDA results [39], relative to the narrow absorption feature α (1^L). For larger samples both the positions of β_1 and β_2 (pluses) and their weighted average (squares) are shown. Comparison with theory indicates that the model accurately reproduces many aspects of the data. Both the splitting between $|N_m| = 2$ and 1^L (the Stokes shift) and the splitting between 1^L and the upper states (1^U and 0^U) are described reasonably well. This result is particularly significant since, although the predicted structure strongly depends on the theoretical input parameters [40], only literature values were used in the theoretical calculation.

Further quantitative evidence for our assignments is obtained from the oscillator

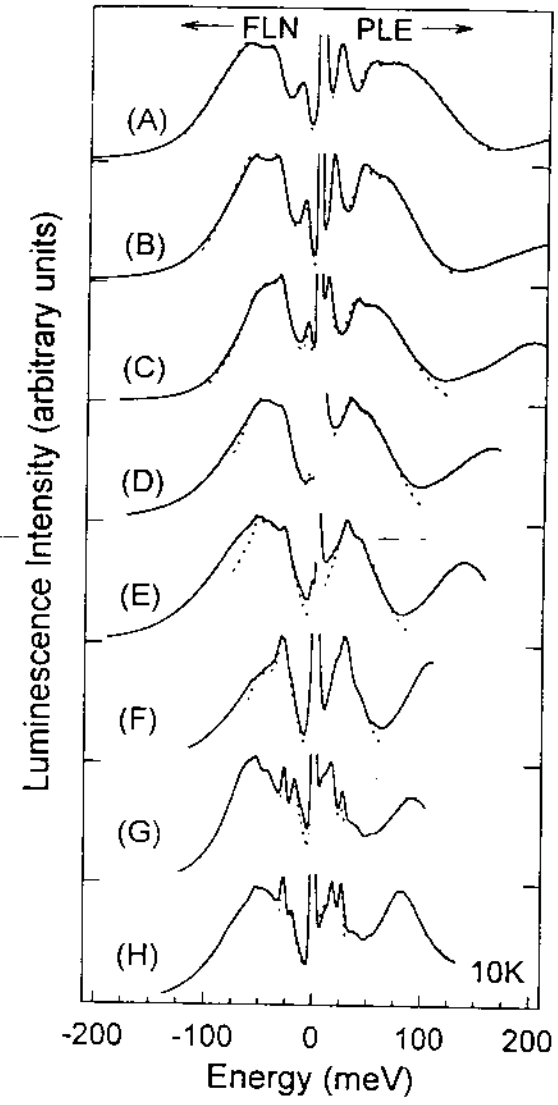

Figure 9.17 The size dependence of band edge fluorescence line narrowing/photoluminescence excitation (FLN/PLE) spectra. In each pair of FLN/PLE results (solid lines) the FLN excitation and the PLE emission energies are the same and indicated by arrows in the full luminescence spectra in Fig. 9.18. The PLE (FLN) data are plotted relative to the emission (excitation) energy. Dotted lines show the best fit used to extract band edge parameters shown in Fig. 9.21. (Adapted from [41].)

strengths of the optically allowed sublevels. In Fig. 9.21(c) the predicted oscillator strength of the optically active sublevels is shown. The strength of the upper states (1^U and 0^U) is combined since these states are not individually resolved in many of our samples. The experimental values are plotted in Fig. 9.21(d). Reasonable agreement between experiment and theory is observed, again with no fitting parameters.

To understand the size dependence of the oscillator strengths we consider two opposing limits. In large dots the states converge to A- and B-like excitons (as in Fig. 9.21a), each possessing half of the total band edge oscillator strength. Therefore, we expect 1^L and the combined upper states (1^U and 0^U) to each approach 0.5 in large sizes. In small dots the exchange interaction dominates and the crystal field and non-spherical shape effects become negligible. In this limit (right hand side of Fig. 9.15)

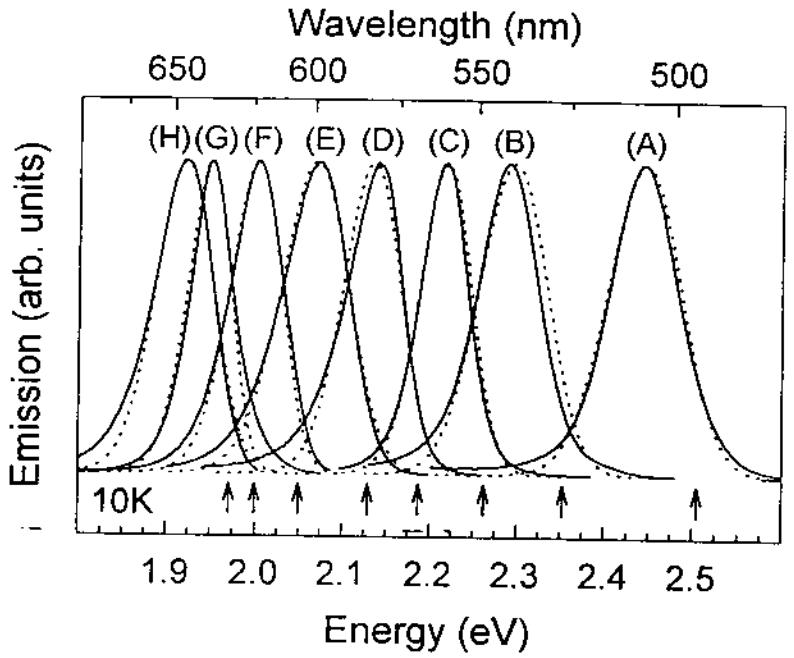

Figure 9.18 Full luminescence spectra for the size series shown in Fig. 9.17 (solid lines). Arrows indicate the fluorescence line narrowing (FLN) excitation positions and photoluminescence excitation (PLE) emission positions (eV). Dotted lines show the best fit used to extract band edge parameters shown in Fig. 9.21. (Adapted from [41].)

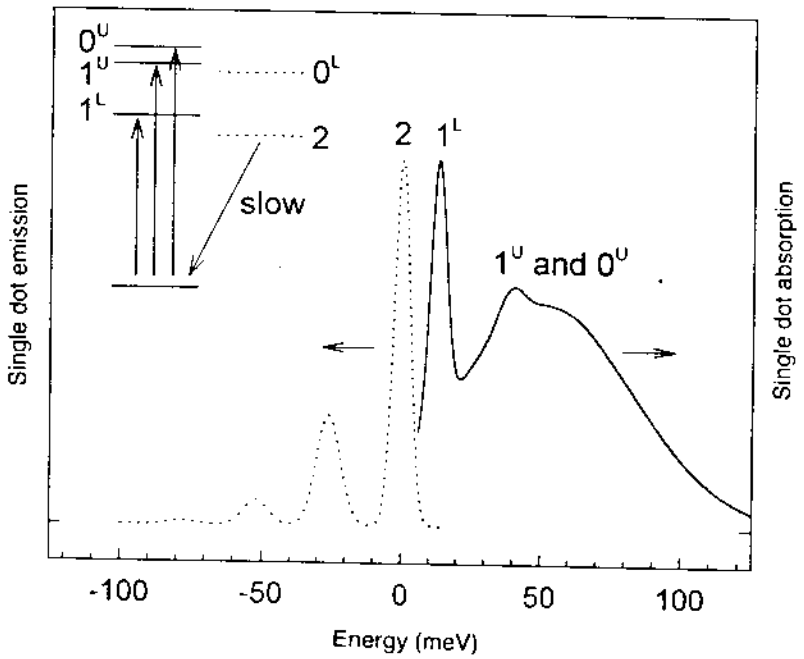

Figure 9.19 Single dot absorption (solid line) and emission (dotted line) structure extracted for the sample shown in Fig. 9.6 including longitudinal optical (LO)–phonon coupling. An energy level diagram illustrates the band edge exciton structure. The sublevels are labelled as in Fig. 9.16. Optically active (passive) levels are shown as solid (dotted) lines. (Adapted from [41].)

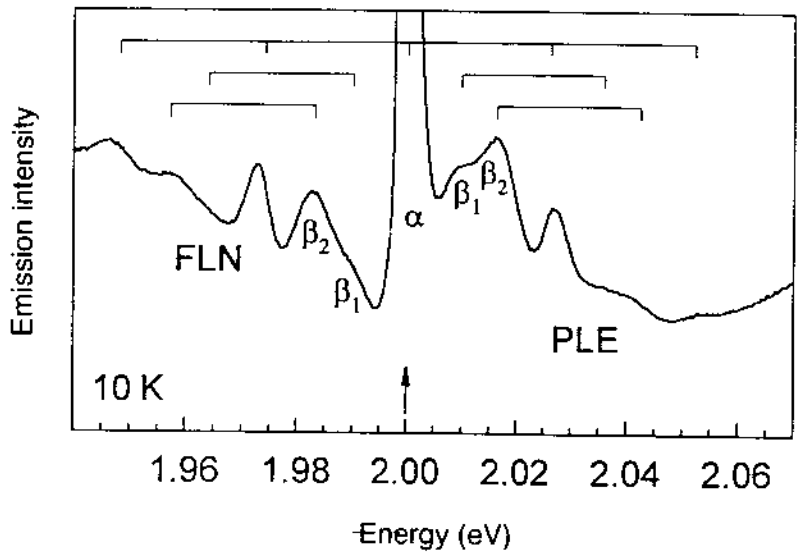

Figure 9.20 Normalized fluorescence line narrowing (FLN) and photoluminescence excitation (PLE) data for a ~44 Å effective radius sample. The FLN excitation and PLE emission energies are the same and are designated by the arrow. Although emission arises from a single emitting state and its LO-phonon replicas, three overlapping LO-phonon progressions are observed in FLN due to the three band edge absorption features (α, β_1 and β_2). Horizontal brackets connect the FLN and PLE and features with their LO-phonon replicas. (Adapted from [41].)

the sublevels converge to the optically forbidden 5-fold degenerate $N = 2$ state, and the optically allowed 3-fold degenerate $N = 1$ state. Since 1^L is correlated to the $N = 2$ state in the large exchange limit, we expect it to be only weakly allowed in small dots. 1^U and 0^U converge to the $N = 1$ state and therefore carry nearly all of the oscillator strength.

2.4.4 EVIDENCE FOR THE 'DARK EXCITON'

Another piece of evidence supporting the existence of the fine structure and its role in the long radiative lifetimes is found in measurements of the emission dynamics. In small dots at cryogenic temperatures the separation between the dark exciton and the 1^L sublevel is large relative to kT. Therefore, as thermalization processes are highly efficient, the photoexcited dot relaxes into the lowest sublevel (the dark exciton). The long (μs) emission is consistent with recombination from this weakly emitting state. Since a strong magnetic field couples the dark exciton to the optically allowed sublevels [40], the emission lifetime should decrease in the presence of a magnetic field. In Fig. 9.22(a) the magnetic field dependence of the emission decays for a ~12 Å radius sample are shown. With increasing magnetic field, the luminescence lifetime clearly decreases. Since the quantum yield remains essentially constant, this result is consistent with the presence of the dark exciton [40].

Another interesting effect of the magnetic field is its influence on the vibrational spectrum. In Fig. 9.22(b) the magnetic field dependence of the FLN spectrum is shown. A dramatic increase in the relative strength of the zero phonon line is observed with increasing field. While this effect is difficult to rationalize within the surface model, it is readily explained by the presence of the dark exciton [40]. In the absence of other relaxation mechanisms the dark exciton would have an infinite lifetime since the

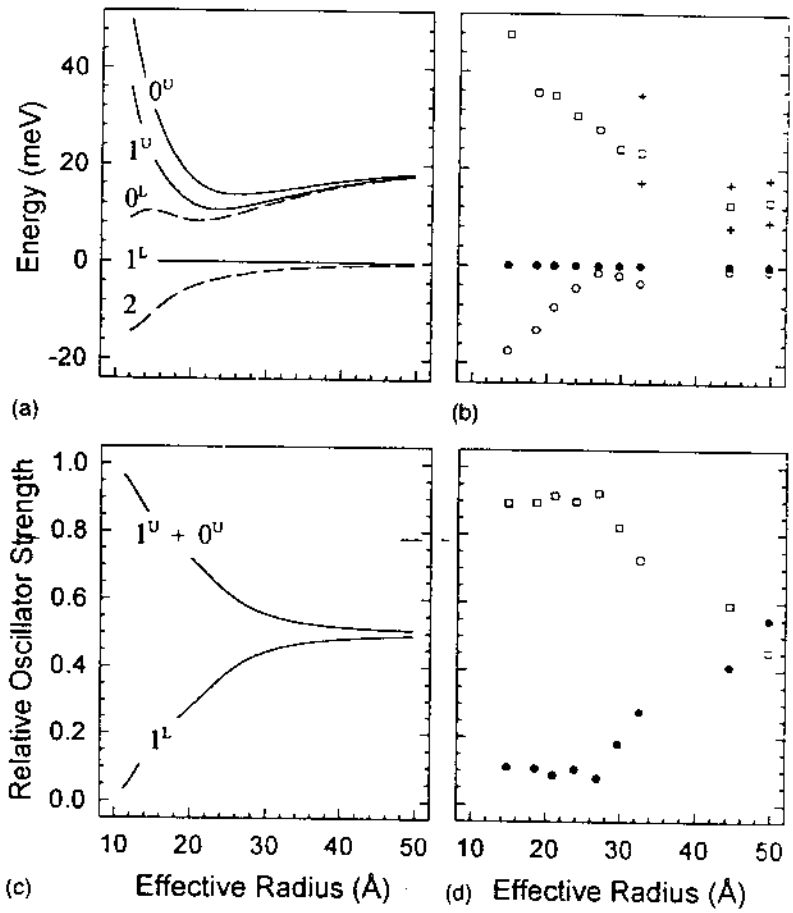

Figure 9.21 (a) Calculated band edge exciton ($1S_{3/2}1S_e$) structure vs effective radius as in Fig. 9.16. (b) Position of the absorbing (filled circles and squares) and emitting (open circles) features from Fig. 9.7 and transient differential absorption spectroscopy (TDA) results from [39]. In samples F–H both the positions of β_1 and β_2 (pulses) and their weighted average (squares) are shown. (c) Calculated relative oscillator strength of the optically allowed band edge sublevels vs effective radius. The combined strength of 1^U and 0^U is shown. (d) Observed relative oscillator strength of the band edge sublevels: 1^L (filled circles) and the combined strength of 1^U and 0^U (squares). (Adapted from [41].)

photon cannot carry an angular momentum of 2 within the electric dipole approximation. However, other less efficient mechanisms are present. For example, the dark exciton can recombine via a LO-phonon-assisted, momentum-conserving transition [74,75]. In this case the higher phonon replicas are enhanced relative to the zero phonon line at zero field. As the field strength is increased the dark exciton becomes partially allowed due to mixing with the optically allowed sublevels. Consequently, the strength of the zero phonon line increases.

2.5 *Summary of CdSe results*

The agreement between theory and experiment shown above indicates that the basic physics behind the absorption and emission behaviour of CdSe quantum dots is understood. The size dependence of the exciton structure and the origin of the

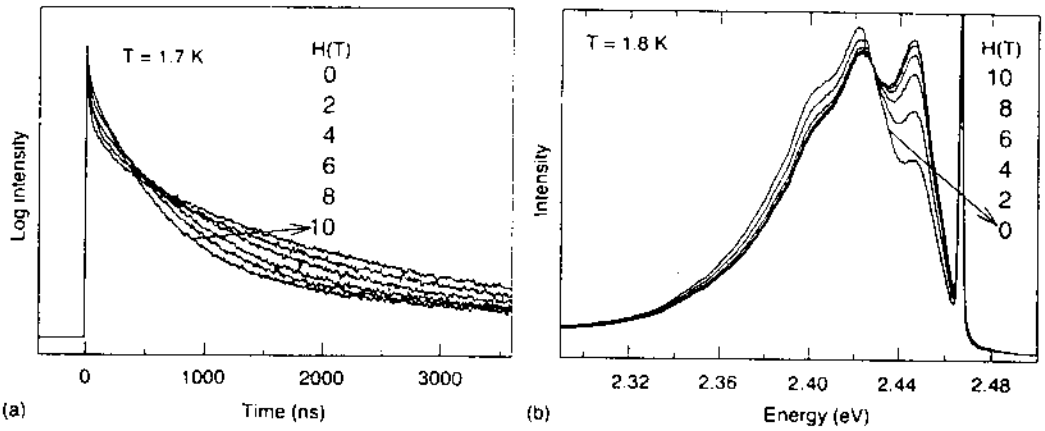

Figure 9.22 Magnetic field dependence of (a) emission decays recorded at the peak of the luminescence (2.346 eV) with an excitation energy of 2.736 eV, and (b) fluorescence line narrowing (FLN) spectra excited at the band edge (2.467 eV) for 12 Å radius dots and normalized to their one phonon line. A small amount of the excitation laser is included to mark the pump position. Experiments were carried out in the Faraday geometry (magnetic field parallel to the light propagation vector). (Adapted from [40].)

long-lived luminescence can now be quantitatively explained by theoretical models. As a prototypical system these explanations may have implications for other quantum confined semiconductor materials. Since the presence of band edge fine structure explains many optical properties previously attributed to surface trapping of the carriers, the role of the surface in the photophysics of these materials is less clear. Whether any discrepancies observed above between experiment and theory can be attributed to the influence of the surface remains an open question.

3 Si quantum dots

3.1 *Radiative rates*

As a result of the extensive work on high quality samples from the Murray *et al.* [5] CdSe synthesis, the spectroscopy of CdSe is well understood. The assignment of the exciton fine structure is proof that the emitting state results from three-dimensional confinement of bulk wurtzite CdSe. The excited state wavefunction is inside the nanocrystal, with a node on the surface in zero order, both before and after structural relaxation between photon absorption and luminescence. In this one case, our level of understanding now approaches that of other classes of large molecules, e.g. aromatic hydrocarbons.

Understanding of Si nanocrystals is far less advanced, and significant questions remain. Investigation of Si is important since this indirect gap material is of overwhelming significance in the electronics and telecommunications industry. Figure 9.23 shows a simplified band structure of Si, which has a diamond lattice. The valence bands are quite similar to those of CdSe (Fig. 9.4), with a maximum at the Brillouin zone centre ($k = 0$). However, the conduction band is different with a minimum at the * point (see Fig. 9.23) near the zone boundary. In Eqn 9.5 the dependence of u_{nk} on k across the Brillouin zone is strong. In the valence bands of both Si and CdSe, u_{nk} is p-like at the zone centre as shown in Fig. 9.11, and develops sp hybridization as k increases. In

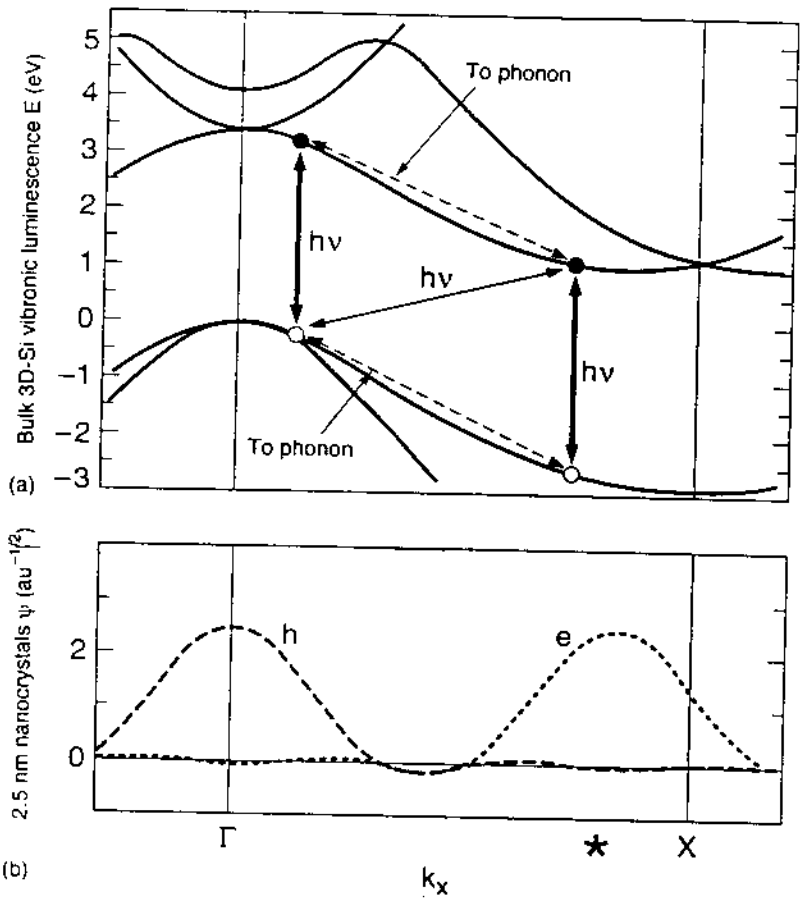

Figure 9.23 (a) Si band structure showing transverse optic (TO) vibronic luminescence mechanism. Broad arrows are allowed transitions, and the narrow arrow is the weak vibronically induced transition; (b) wavevector distributions for confined electron and hole in 2.5 nm nanocrystal, adapted from [76].

CdSe, the conduction band is s-like and nearly isotropic at the zone centre, and thus the direct gap transition is p- to s-like within the unit cell. Optical excitation is a type of charge transfer transition from a p orbital on Se to an empty s orbital on Cd. In covalent Si, the conduction minimum at * is an sp hybrid along a 001 direction. It is 6-fold spatially degenerate in view of the possible directions (including sign) of k. If one considers additionally the spin and valence band degeneracies previously described for CdSe, then the lowest indirect gap exciton is 48-fold degenerate. A complex exciton fine structure, dependent upon both shape and size, should be present.

Non-vertical electronic transitions of bulk Bloch states, such as that across the Si indirect gap in Fig. 9.23, are forbidden under dipole selection rules because of the phase difference between electron and hole wavefunctions from one unit cell to the next. This selection rule is a consequence of k being an exact quantum number in an infinite periodic lattice. In a finite nanocrystal, k is not exact and the transition becomes weakly dipole allowed. Figure 9.23(b) shows the Fourier wavevector superpositions necessary to localize an electron or hole inside a 2.5 nm diameter Si nanocrystal [76]. The tails of the two distributions overlap, and this is the source of the purely electronic transition dipole which should develop in small nanocrystals.

Just as in molecules, and in the forbidden $N = 2$ component of CdSe nanocrystals

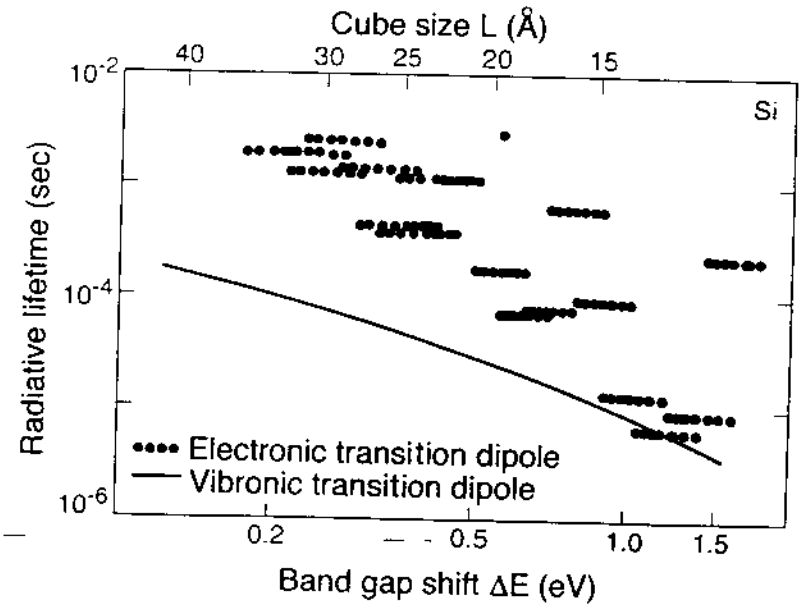

Figure 9.24 Purely electronic radiative lifetimes (dots) and vibronic radiative lifetimes (line) vs size on upper axis. For a given size, several lifetimes are possible depending upon shape, as shown in [76].

discussed above, a forbidden electronic transition can be weakly vibronically allowed through participation of a symmetry-lowering vibration. In bulk crystalline Si the transition is vibronically induced by a transverse optic (TO) vibration that compensates for the k mismatch, as shown in Fig. 9.23. In bulk semiconductors, electron–phonon coupling is generally weak because of the delocalized nature of the wavefunctions, and especially weak in non-polar Si. Simple theories of quantum confinement predict the coupling increases as d^{-3} in nanocrystals, as the wavefunctions become more compact [77]. Thus vibronically induced emission, which occurs in parallel to electronic emission, is also predicted to increase in nanocrystals, as shown in Fig. 9.24. Emission rates are a function of shape as well as size, because of the directional degeneracy of the confined electron. In this calculation, the transition is predicted to remain an indirect gap — that is, the vibronic rate dominates the purely electronic rate — down to the smallest sizes near 1.5 nm [76].

For comparison one might consider the hydrogenic exciton of bulk Si, bound by the weak, screened Coulomb attraction between electron and hole at liquid helium temperatures. In this species, about 3 nm in diameter, the transition is experimentally indirect with a singlet, vibronically induced luminescence rate Γ_r of 2×10^4 s^{-1} [78,79]. This is a slow rate — somewhat longer than the vibronically induced fluorescence rates of the lowest excited states of formaldehyde and benzene, and the $N = 2$ component of CdSe. An allowed transition, such as in the $N = 1$ CdSe component, would have a rate near 10^9 s^{-1}.

3.2 *Porous silicon*

Much of the interest in Si nanocrystals luminescence comes from the recent discovery

of quantum confinement properties and high yield photoluminescence in porous Si thin films [80–83]. As schematically shown in Fig. 9.25, anodic electrochemical etching of wafer Si in alcoholic HF solution creates a yellowish surface film of micron thickness. Etching occurs as holes flow to the wafer surface and oxidize surface Si atoms in contact with HF. This film is composed of an open, irregular network of Si wires with undulating diameter, and/or Si nanocrystals partially fused to their neighbours. The etching process naturally creates electrically passivating H atom termination on newly uncovered surface Si atoms. Eighty per cent porous films have larger optical band gaps than the 1.1 eV band gap of bulk Si, and show efficient red photoluminescence near 2.0 eV. The typical particle size is in the 1–10 nm range, and these optical effects are attributed to quantum confinement. The high luminescence yield naturally suggests the idea that porous Si light-emitting diodes could be grown on Si microcircuits, and has attracted widespread industrial interest.

The electrochemical properties of these films are especially interesting. Lehmann and Goselle originally proposed that the etching process is self-terminating in the quantum confinement size regime [84]. Electrochemical etching stops when the hole confinement energy in a nanocrystal becomes larger than the bulk Si hole energy at a particular applied voltage. Etching alternately can occur for holes generated by direct light absorption in the film, and here the final size can be controlled by the wavelength of the optical excitation. Porous Si liquid junction cells show strong electroluminescence with appropriate electron injecting redox carriers in the electrolyte [85–89]. The colour is voltage tunable, apparently as the Fermi level moves across the nanocrystal electron

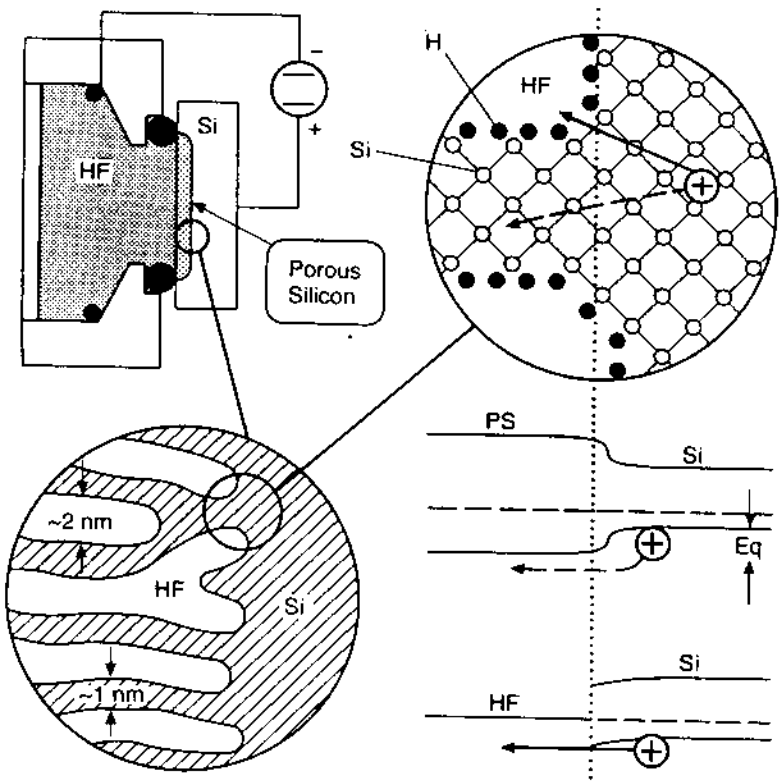

Figure 9.25 Structural and electronic schematic diagram of porous Si films on Si crystal, adapted from [93].

affinity size distribution in the porous-Si film. For all these reasons, as well as the possibility of new electronic devices made from nanometer scale Si, there is considerable interest in understanding the properties of individual Si nanocrystals.

3.3 SILICON NANOCRYSTAL GENERATION AND CHARACTERIZATION

At present the preparation of Si nanoparticles is primitive with respect to the Murray *et al.* CdSe organometallic synthesis. The situation is somewhat similar to the state of experimentation a decade ago in the CdSe work. Si nanocrystals with a passivating oxide surface layer about 0.8 nm thick have been made in a two-stage aerosol apparatus operating near 1000°C [90]. Gaseous disilane is thermally decomposed in about 1.5 atm of flowing He gas. Diamond lattice Si particles nucleate, grow, anneal, and become faceted at such temperatures in the gas phase. They are then briefly (30 ms) oxidized, cooled while flowing, and collected as a colloid in ethylene glycol. There is no size control except through the initial concentration of disilane, and a wide size distribution is made. High pressure liquid chromatography and size-selective precipitation methods are used to partially narrow the distribution for optical experiments [91]. For example, Fig. 9.26 shows broad luminescence spectra and size distributions of two fractions created by size-selective precipitation, from a Si nanocrystal colloid that initially showed photoluminescence in the 600–900 nm range. In bulk Si crystals, band gap luminescence occurs weakly at about 1120 nm. One fraction contains smaller single

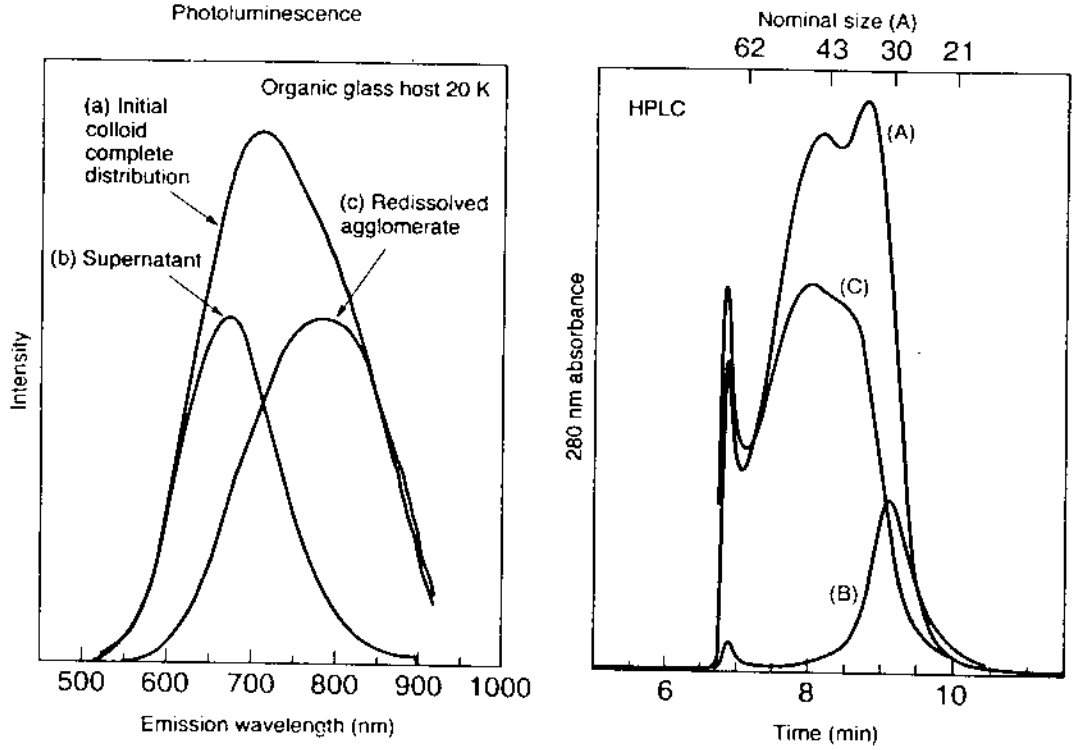

Figure 9.26 Left hand side: spectrally corrected Si nanocrystal luminescence spectra in organic glass (350 nm excitation wavelength, 20 K). Right hand side: corresponding HPLC chromatograms with approximate logarithmic size calibration. Relative intensities are arbitrary, as adapted from [91].

nanocrystals and emits at 650 nm in the red. The absolute quantum yield of this sample is 5.8% at room temperature, increasing to near 50% below 50 K. The other fraction contains larger nanocrystals, and aggregates, and emits near 800 nm.

Physical characterization is difficult. In larger nanocrystals direct TEM imaging is possible, but in smaller particles the contrast is poor. Si K shell X-ray near-edge absorption data in smaller nanocrystals that emit near 2.0 eV confirm the Si core oxide shell structure, and show a 1.2–1.5 nm Si core diameter [92]. The total diameter including oxide is about 2.5 nm. The identification and characterization of Si particles below 2.5 nm in diameter remains a very difficult problem. Such particles are especially difficult to detect in the presence of larger Si particles.

Ethylene glycol nanocrystal colloids are optically clear, and relatively crack-free organic glasses with embedded Si nanocrystals can be made by freezing between sapphire plates. In CdSe optical characterization, hole burning (TDA) and size-selective PLE and FLN methods probe optical properties within the size distribution. The band edge exciton oscillator strength is so small in Si that a direct hole burning experiment would be very difficult. However, photoexcitation experiments are feasible due to the high luminescence quantum yield. Figure 9.27 shows that the PLE excitation spectrum of 600 nm luminescence at ~15 K is a featureless, monotonically increasing continuum, characteristic of an indirect gap material with band gap the same as the monitored 600 nm luminescence wavelength [93,94]. This spectrum actually shows less structure than the equivalent, calculated spectrum for bulk diamond lattice Si, in that

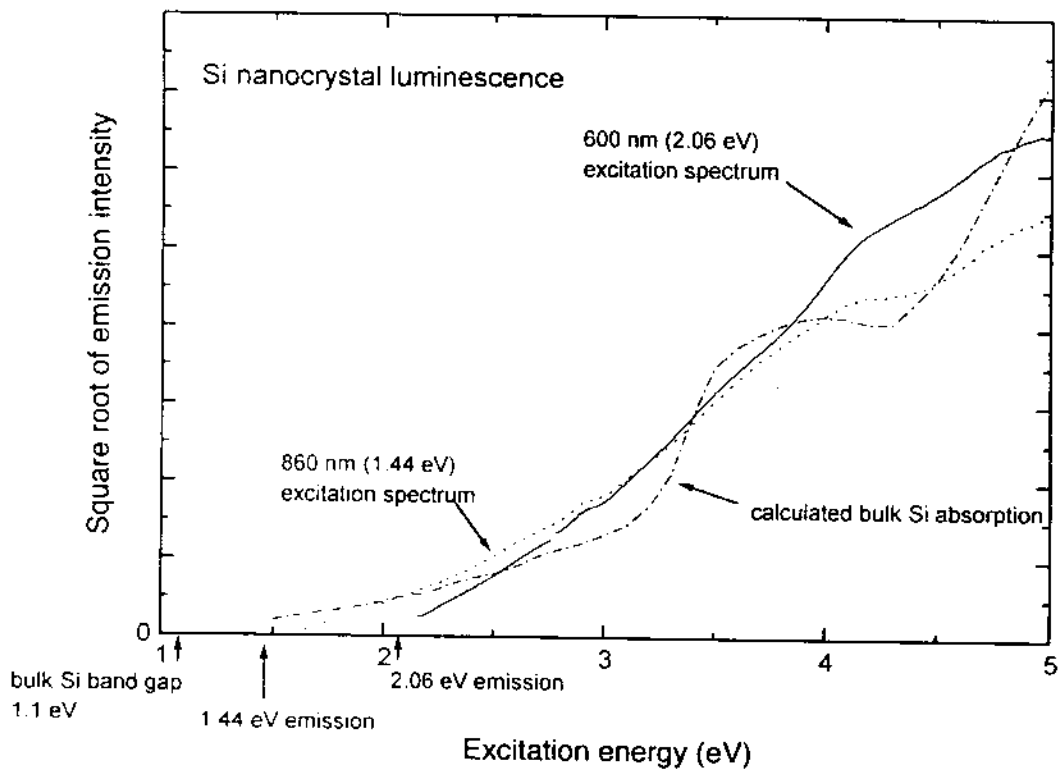

Figure 9.27 Square root of 600 nm and 860 nm luminescence intensity from Si nanocrystals at ~15 K as a function of excitation radiation energy. For comparison, the figure also shows the square root of the optical absorption cross-section of a small Si sphere calculated from the electric dipole term of Mie theory using bulk Si dielectric constant data, as adapted from [93].

the broad ultraviolet feature due to the 3.4 eV direct gap is almost washed out in nanocrystals. This result should be contrasted with the equivalent Figs 9.6(b) and 9.7(b), which shows discrete structure in CdSe. In contrast to Si, CdSe nanocrystals show more discrete structure than bulk CdSe.

The ultraviolet-excited, full photoluminescence spectrum is a broad featureless band, peaking near 700 nm in the particular sample in Fig. 9.28. As in CdSe, possible structure is obscured by sample size broadening. CW laser excitation at 710 nm excites luminescence from just the larger nanocrystals in the distribution, and this spectrum is narrower and exhibits partial TO phonon structure. However, this photoluminescence structure is different from the strong emission observed just below the laser excitation line for CdSe nanocrystals in Fig. 9.6. In Si the luminescence is weak near the laser excitation energy, and increases for Stokes shifts of 1 and 2 TO phonons.

This difference is a signature of the difference between a direct and indirect gap transition. In Si the luminescence data can be fit, as a function of excitation wavelength, by a near-Gaussian band gap-size distribution centred at 650 nm, and a single

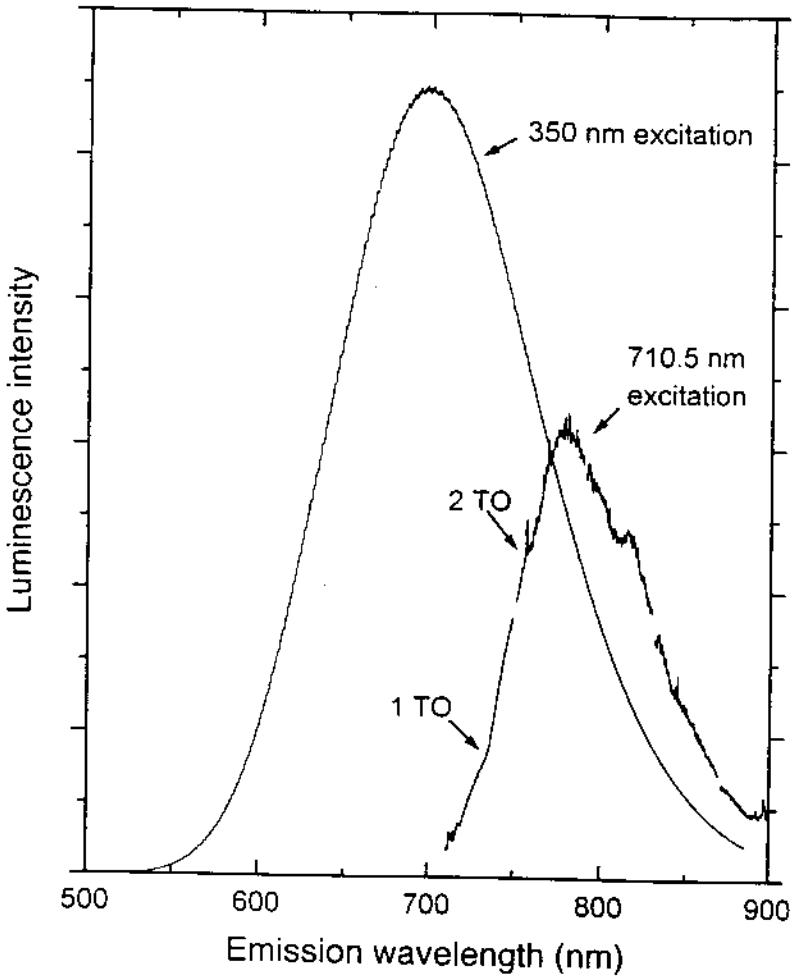

Figure 9.28 Comparison of the 350 nm excited, low resolution emission spectrum of Si nanocrystals at ~15 K, and the higher resolution (0.2 nm) emission spectrum excited at 710.5 nm. Weak thresholds are observed at one and two times the transverse optic (TO) phonon frequency in the 710.5 spectrum, as adapted from [93].

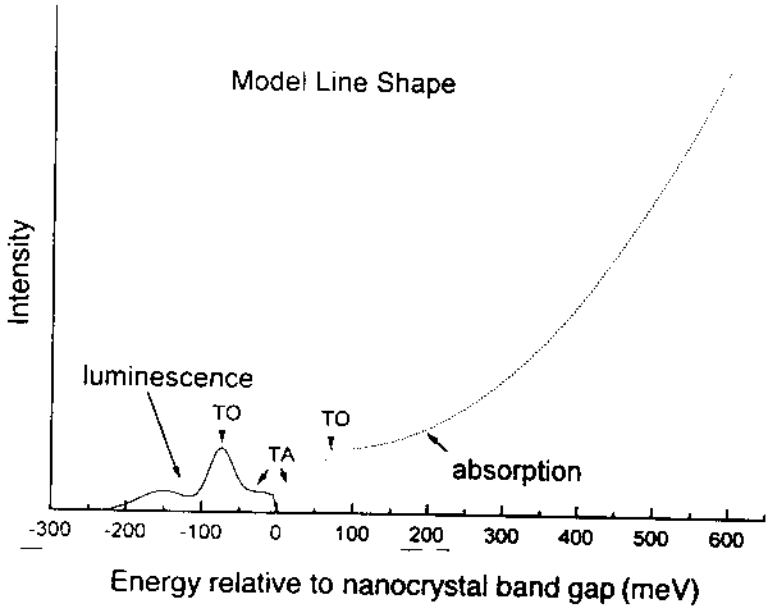

Figure 9.29 Si single nanocrystal model luminescence and absorption spectra, derived from fitting spectroscopic data in [93]. The zero of energy corresponds to the exciton energy of the single nanocrystal.

nanocrystal spectrum as shown in Fig. 9.29. The strongest features are TO vibronic features present in both absorption and emission. There is a weaker vibronic feature in the TA phonon position, and essentially no intensity on the band gap zero phonon line. In absorption there is also rising continuous absorption that corresponds to absorption into the higher electronic states of an indirect gap material. The spectra and assignments are very similar to those of p-Si [75,95,96], and confirm the indirect gap nature of Si nanocrystals emitting near 650 nm. This spectrum should be compared with the CdSe single dot spectrum in Fig. 9.19.

The lifetimes are very long; the 630 nm lifetime τ increases from $\sim 5 \times 10^{-5}$ s at 293 K to $\sim 2.5 \times 10^{-3}$ s at 20 K [91]. In CdSe the lifetime is on the order of 10^{-8} s at 293 K. In a molecule, or in a nanocrystal with just one electron–hole pair, the decay rate (inverse lifetime) is $\tau^{-1} = \Gamma_r + \Gamma_{nr}$. The first term is the radiative rate, and the second term is the competing non-radiative rate. The luminescence quantum yield is defined by $QY = \Gamma_r / (\Gamma_r + \Gamma_{nr})$. From measurement of both QY and τ, both Γ_r and Γ_{nr} are determined as a function of temperature. At 20 K, Γ_{nr} is negligible with respect to Γ_r, which itself is quite slow, $\sim 10^3\ s^{-1}$. Γ_r increases by an order of magnitude as temperature increases to about 150 K, and then plateaus. Γ_{nr} increases by several orders of magnitude as temperature increases, so at room temperature the quantum yield has decreased to $\sim 5\%$. In both p-Si and nanocrystal Si, the non-radiative process is not understood.

3.4 *Photophysics analysis, and comparison with bulk crystalline Si*

The indirect gap nature of the spectra, the absence of a significant Stokes shift beyond the TO thresholds, the very long lifetimes, and the similarity of hydride and oxide terminated nanocrystal/porous Si data, all support assignment of the red luminescence

to the volume-confined band gap exciton, just as in CdSe. There are some differences between predicted and observed properties. Present theory predicts a diameter larger by a factor of 2 than the 1.2–1.5 nm size deduced for nanocrystals emitting near 2.0 eV [97–99]. Also, the very long radiative rates described above appear to be even longer than predicted for volume-confined indirect excitons. Perhaps the wavefunction is polarized by a rough surface or non-spherical shape in some way we do not presently understand. Distributions of shape and surface roughness will obscure the data in laser excitation spectra. In fact, close analysis of the present Si nanocrystal spectra shows partially resolved sharp phonon transitions in the TO phonon regions. Improved syntheses and methods are needed in order to obtain high quality fine structure data as described above for CdSe.

At liquid helium temperatures, the Coulombic exciton in bulk Si has similarities to the quantum confined electron–hole pair in a nanocrystal. Both are spatially confined systems, yet both are indirect with radiative lifetimes at least 10^4 longer than that of an allowed transition. In both cases the competing multiphonon radiationless transition Γ_{nr} is negligible, and the quantum yield of luminescence, once the bound pair is formed, is near unity. Multiphonon internal conversion, of the type often seen in molecules, is slow as a consequence of the weak electron–phonon coupling found in a covalent, strongly bound, defect-free lattice.

At room temperature, however, bulk crystalline Si is fundamentally different from nanocrystal Si. In bulk Si, electron–hole pairs dissociate, and the ensemble of individual carriers interact. The carriers are mobile over macroscopic distances, and recombination can be efficiently catalysed by defects and impurities present in very low concentrations. In the perfect lattice, all recombination processes are slow, and carriers at very low densities live as long as 40 ms at 293 K [100]. At normal carrier densities, however, the recombination process is the three-body electronic non-radiative Auger process

$$e + h + (e \text{ or } h) \rightarrow (e \text{ or } h) \tag{9.23}$$

with 1.1 eV of kinetic energy. The third carries away the band gap recombination energy, and then rethermalizes. This process shortens the effective lifetime by orders of magnitude.

The luminescence quantum yield increases in nanocrystal Si and porous Si at 293 K, not because Γ_r increases, but because Γ_{nr} decreases, with respect to bulk crystalline Si. In a material made of well-passivated Si nanocrystals, an electron–hole pair in one nanocrystal is electrically isolated from pairs in other nanocrystals, and the Auger process is significantly decreased. In addition, a rare impurity or lattice defect can only quench luminescence in one nanocrystal. In nanocrystal Si, an electron and hole are superimposed for long periods of time, not by their Coulomb attraction but by confinement. Because the pair remains spatially superimposed, and competing non-radiative processes are depressed, the QY is far larger in nanocrystal Si than in bulk Si. In almost any electronic material, photoluminescence increases as mobility decreases.

This work allows us to recognize nanocrystal size regimes in Fig. 9.30. Spectroscopic properties can be broken into molecular, quantum dot (e.g. nanocrystal), polariton, and bulk regions. These labels represent the evolution of molecular to unit cell structures, discrete electronic states to continuous bands, and weak dipole scattering into strong

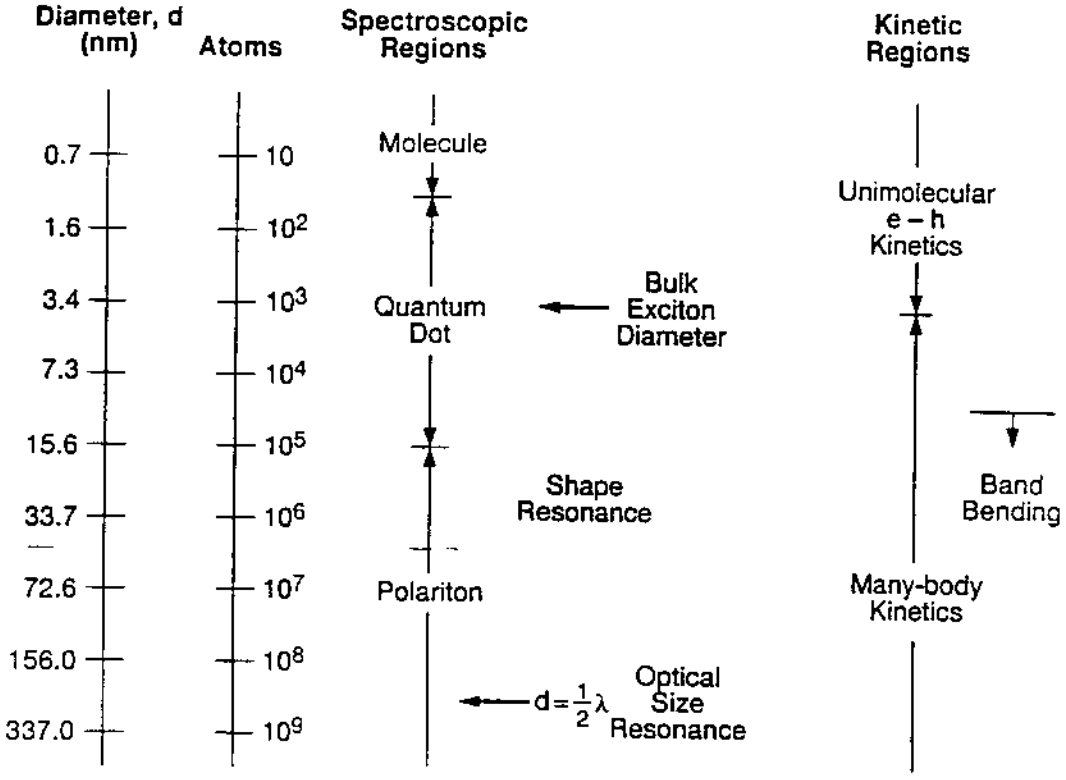

Figure 9.30 Schematic representation of size regimes used for describing spectroscopic and excited state kinetic properties of semiconductor nanocrystals, as adapted from [93].

polariton electromagnetic scattering. Bulk optical properties appear only when size is much larger than an optical wavelength.

In the nanocrystal or quantum dot regime, CdSe nanocrystals show discrete excited state optical absorption, while in Si the optical absorption is continuous. Two effects contribute to this difference: first, the spacing of quantized conduction band states is much larger in CdSe than in Si, because of the very small CdSe electron effective mass $\sim 0.11\ m_e$. Second, in CdSe only a few transitions, out of the many possible, appear strongly because of electric dipole selection rules. In Si, all possible transitions appear to be present at similar intensity due to vibronic interaction. In Si the discrete yet dense spectrum appears continuous, as individual transitions overlap with respect to their line widths, at least in the present Si nanocrystal samples. Comparison of rock salt (indirect) and wurtzite (direct) CdSe spectra leads quite unambiguously to a similar conclusion [101].

This work on Si, and previous work on AgBr nanocrystals [102–106], show that size regimes exist in kinetic properties as well. At typical excitation intensities, large crystallites contain several dissociated pairs and exhibit many interacting carrier recombination kinetics. Small nanocrystals can exhibit size exclusion of bulk lattice defects and impurities, and also do not show surface band bending if dopants are excluded due to small size. Unexcited small nanocrystals are intrinsic dielectric particles. At typical excitation intensities, unimolecular decay of a single, quantum confined electron–hole pair is observed.

3.5 *Electron affinities and transport in nanocrystal materials*

If a nanocrystal contains an extra electron and thus has a net charge, an electric field exists in the nanocrystal and interacts with the local environment. In p-Si of high porosity this external field dominates both single nanocrystal energetics [2,3,107–112] and transport phenomena [113], and provides a way of 'tuning' the transport behaviour via the polarity of the media in the pores. The electron affinity of a Si nanocrystal decreases by ΔA from the approximately 4.5 eV affinity of an electron on the conduction band edge in bulk Si:

$$\Delta A = KE(d) + \langle 1S|P(r)|1S\rangle. \tag{9.24}$$

$KE(d)$ is the kinetic energy, which can be treated by the effective mass approximation in the simplest approximation. The second term is the loss of dielectric polarization energy, averaged over a 1S wave function in the nanocrystal; it tends to be larger than $KE(d)$ if the local environment has a low dielectric constant. The second term can be approximated as [110]

$$\langle 1S|P(r)|1S\rangle \cong \left(\frac{e^2}{d}\right)\left(\frac{1}{\varepsilon_{out}} - \frac{1}{\varepsilon_{Si}}\right) + \delta\Sigma. \tag{9.25}$$

Here ε_{out} refers to the medium outside the nanocrystal, and

$$\delta\Sigma = \frac{0.94e^2}{\varepsilon_{Si}d}\left(\frac{\varepsilon_{out}\varepsilon_{Si}}{\varepsilon_{out} + \varepsilon_{Si}}\right). \tag{9.26}$$

Transport in p-Si can be modelled as the hopping of electrons among touching nanocrystals of variable diameter. If an electron jumps from a 2 nm Si nanocrystal to a 4 nm nanocrystal in vacuum, the exothermicity is

$$\Delta G = \Delta A(4\text{ nm}) - \Delta A(2\text{ nm}) = -0.5\text{ eV}, \tag{9.27}$$

which must be dissipated in some coupled 'vibrational' degree of freedom.

In Si an electron is weakly coupled to Si acoustic modes by the deformation potential. The internal acoustic reorganization energy λ is small — for 2 nm Si, λ is only ~12 meV. The external λ for water polarization (if present) outside the nanocrystal is much larger, ~400 meV [113]. In the Marcus theory of solvent influence on kinetics, the electron hopping rate at room temperature is

$$k(s^{-1}) \propto \exp(-G_{act}/kT), \tag{9.28}$$

where the activation energy is given by [114–116]

$$G_{act} = (\lambda + \Delta G)^2/4\lambda. \tag{9.29}$$

For fast, activationless transfer, the negative exothermicity ΔG must equal the total λ, which is positive. Thus for fast electron transfer from a 2 nm to a 4 nm nanocrystal, λ must be ~0.5 eV.

Figure 9.31 is a plot of $\log(k)$ vs the diameter of the electron accepting nanocrystal, for a fixed 2 nm donor size. For a 2 nm acceptor in vacuum, the transfer is resonant and

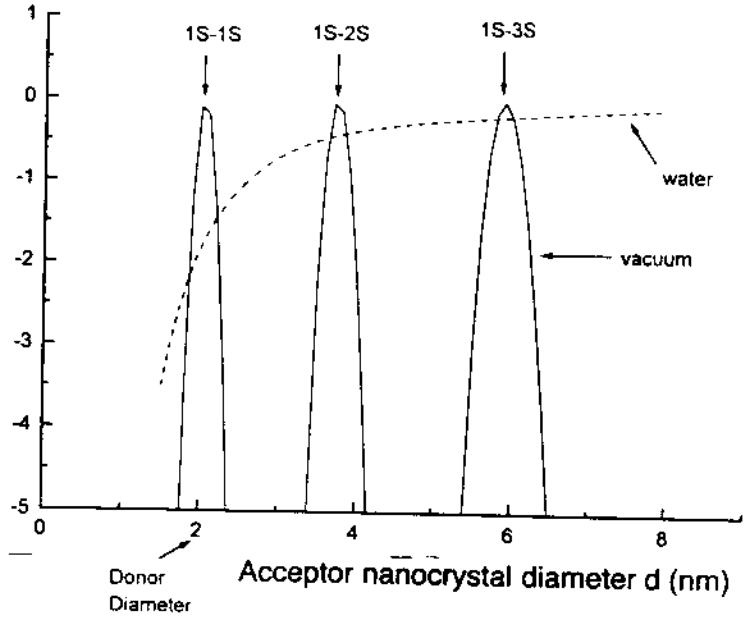

Figure 9.31 Log of the unimolecular electron hopping rate in water and in vacuum, for a 2 nm Si donor nanocrystal, as a function of acceptor nanocrystal size, as adapted from [113].

the rate is fast. It is also fast for specific larger sizes where resonant transfer to excited 2*S* and 3*S* states is possible. For other sizes transfer is very slow due to a huge activation energy as λ is small. In water where λ is large, the resonant nature of transfer is lost. In water, transfer is fast for all cases except resonant transfer between nanocrystals of equal size. In this case, the polarization of the water around the initial nanocrystal tends to 'self-trap', or stabilize, the carrier. Interstitial water has a huge enabling effect on electron hopping, if the material is highly porous and the size distribution is rather wide. Water also has a major effect on electron injection into a nanocrystal already containing a hole, creating an exciton which then may decay radiatively. In this process two charged nanocrystals convert into two neutral nanocrystals, and a large polarization energy is dissipated during injection.

General speaking, dry p-Si behaves electrically like a resonant tunnelling device. However, wet p-Si shows fast, non-resonant electron transfer similar to that commonly seen in biological and molecular processes in polar environments. This Marcus solvation effect on kinetics demonstrates yet another molecule-like property of nanocrystals.

4 Concluding remarks

Most nanocrystal research in the past has focused on understanding the chemistry and physics of individual nanocrystals. We now can outline, in broad form, the evolution from molecular properties at small size to solid-state properties at large size. In the coming decade, synthetic methods should improve to yield high quality nanocrystals of all major semiconductors, in gram amounts with controlled and variable surface chemistry, as is presently the situation with CdSe. Nanocrystals are new classes of large molecules in the context of chemistry. In the context of molecular electronics, nanocrystals are building blocks. Our challenge is to now invent new nanometre devices with

unique properties, that go beyond the 'canonical' devices — diodes, transistors, and wires — that industry already knows how to miniaturize, organize, and assemble very efficiently. New functionality can alternately come from new material properties. New materials made with nanocrystals are now appearing. Inexpensive, large area solar cells have been made from porous TiO_2 with a liquid junction [117]. The combination of nanocrystals with conductive organic polymers promises to significantly increase design possibilities in photovoltaic and electroluminescent diodes [118–120]. Finally, the crystallization of nanocrystals into opal-like structures [26] promises to create a new class of semiconducting materials with properties tunable via interstitial doping, surface chemistry, and nanocrystal size. This area of materials science should have a rich future.

Acknowledgements. The work presented in this review is the result of a number of collaborations. D.J.N. and M.G.B. especially thank our colleagues Al. L. Efros, C.B. Murray, and M. Nirmal, who have contributed significantly to the results described. L.E.B. gratefully acknowledges a continuous, stimulating collaboration with many excellent colleagues at AT&T Bell Laboratories over the past decade. Much of the nanocrystal research at Murray Hill was performed by former post-doctoral fellows: J.J. Macklin, K.A. Littau, M.G. Bawendi, and A.P. Alivisatos. D.J.N. benefited from fellowships from NSF and Arthur D. Little. M.G.B. thanks the Lucille and David Packard Foundation and the Alfred P. Sloan Foundation for fellowships. This work was funded in part by the NSF-MRSEC program (DMR-94-00034), by the NSF (DMR-91-57491), and by AT&T Bell Laboratories.

5 References

1 Efros AlL, Efros AL. *Sov Phys Semicond* 1982; **16**: 772.
2 Brus LE. *J Chem Phys* 1983; **79**: 5566.
3 Brus LE. *J Chem Phys* 1984; **80**: 4403.
4 Pankove JI. *Optical Processes in Semiconductors.* New York: Dover, 1971: Ch. 3.
5 Murray CB, Norris DJ, Bawendi MG. *J Am Chem Soc* 1993; **115**: 8706.
6 Flügge S. *Practical Quantum Mechanics*, Vol. 1. Berlin: Springer, 1971: 155.
7 Kittel C. *Introduction to Solid State Physics.* New York: Wiley, 1986: Ch. 8.
8 Bastard G. *Wave Mechanics Applied to Semiconductor Heterostructures.* New York: Wiley, 1988.
9 Altarelli M. In: Stella A, ed. *Semiconductor Superlattices and Interfaces.* Amsterdam: North Holland, 1993: 217.
10 Bányai L, Koch SW. *Semiconductor Quantum Dots.* Singapore: World Scientific, 1993.
11 Xia JB. *Phys Rev B* 1989; **40**: 8500.
12 Hellwege KH, ed. *Landolt-Bornstein Numerical Data and Functional Relationships in Science and Technology, New Series, Group III*, Vol. 17b. Berlin: Springer-Verlag, 1982.
13 Aven M, Prener JS. *Physics and Chemistry of II–VI Compounds.* Amsterdam: North Holland, 1967: 41.
14 Kittel C. *Quantum Theory of Solids.* New York: Wiley, 1987: Chs 9, 14.
15 Kane EO. *J Chem Phys Solids* 1957; **1**: 249.
16 Kane EO. In: Zawadzki W, ed. *Narrow Band Semiconductors. Physics and Applications. Lecture Notes in Physics*, Vol. 133. Berlin: Springer Verlag, 1980.
17 Luttinger JM, Kohn W. *Phys Rev* 1955; **97**: 869.
18 Luttinger JM. *Phys Rev* 1956; **102**: 1030.

19 Bir GL, Pikus GE. *Symmetry and Strain-Induced Effects in Semiconductors*. New York: Wiley, 1974.
20 Lipari NO, Baldereschi A. *Phys Rev Lett* 1970; **42**: 1660.
21 Baldereschi A, Lipari NO. *Phys Rev B* 1973; **8**: 2697.
22 Ge'lmont BL, D'yakonov MI. *Sov Phys Semicond* 1972; **5**: 1905.
23 Bowen Katari JE, Colvin VL, Alivisatos AP. *J Phys Chem* 1994; **98**: 4109.
24 Hines MA, Guyot-Sionnest P. *J Phys Chem* 1996; **100**: 468.
25 Kagan CR, Murray CB, Nirmal M, Bawendi MG. *Phys Rev Lett*, 1996; **76**: 1517.
26 Murray CB, Kagan CR, Bawendi MG. *Science* 1995; **270**: 1335.
27 Ekimov AI, Efros AlL, Onushchenko AA. *Solid State Commun* 1985; **56**: 921.
28 Ekimov AI, Onushchenko AA. *JETP Lett* 1984; **40**: 1136.
29 Rossetti R, Hull R, Gibson JM, Brus LE. *J Chem Phys* 1985; **82**: 552.
30 Ekimov AI, Onushchenko AA, Efros AlL. *JETP Lett* 1986; **43**: 376.
31 Chestnoy N, Hull R, Brus LE. *J Chem Phys* 1986; **85**: 2237.
32 Alivisatos AP, Harris AL, Levinos NJ, Steigerwald ML, Brus LE. *J Chem Phys* 1988; **89**: 4001.
33 Ekimov AI, Efros AlL, Ivanov MG, Onushchenko AA, Shumilov SK. *Solid State Commun* 1989; **69**: 565.
34 Wang Y, Herron N. *Phys Rev B* 1990; **42**: 7253.
35 Bawendi MG, Wilson WL, Rothberg L *et al. Phys Rev Lett* 1990, **65**: 1623.
36 Peyghambarian N, Fluegel B, Hulin D *et al. IEEE J. Quantum Electron* 1989; **25**: 2516.
37 Esch V, Fluegel B, Khitrova G *et al. Phys Rev B* 1990; **42**: 7450.
38 Ekimov AI, Hache F, Schanne-Klein MC *et al. J Opt Soc Am B* 1993; **10**: 100.
39 Norris DJ, Bawendi MG. *J Chem Phys* 1995; **103**: 5260.
40 Nirmal M, Norris DJ, Kuno M, Bawendi MG, Efros AlL, Rosen M. *Phys Rev Lett* 1995; **75**: 3728.
41 Norris DJ, Efros AlL, Rosen M, Bawendi MG. *Phys Rev B*, 1996; **53**: 16347.
42 Hilinski EF, Lucas PA, Wang Y. *J Chem Phys* 1988; **89**: 3435.
43 Roussignol P, Ricard D, Flytzanis C, Neuroth N. *Phys Rev Lett* 1989; **62**: 312.
44 Peyghambarian N, Fluegel B, Hulin D *et al. IEEE J Quantum Electronics* 1989; **QE-25**: 2516.
45 Park SH, Morgan RA, Hu YZ, Lindberg M, Koch SW, Peyghambarian N. *J Opt Soc Am B* 1990; **7**: 2097.
46 Esch V, Fluegel B, Khitrova G *et al. Phys Rev B* 1990; **42**: 7450.
47 Kang KI, Kepner AD, Gaponenko SV, Koch SW, Hu YZ, Peyghambarian N. *Phys Rev B* 1993; **48**: 15449.
48 Kang K, Kepner AD, Hu YZ *et al. Appl Phys Lett* 1994; **64**: 1487.
49 Alivisatos AP, Harris AL, Levinos NJ, Steigerwald ML, Brus LE. *J Chem Phys* 1988; **89**: 4001.
50 Woggon U, Gaponenko S, Langbein W, Uhrig A, Klingshirn C. *Phys Rev B* 1993; **47**: 3684.
51 Gaponenko SV, Woggon U, Saleh M *et al. J Opt Soc Am B* 1993; **10**: 1947.
52 Norris DJ, Nirmal M, Murray CB, Sacra A, Bawendi MG. *Z Phys D* 1993; **26**: 355.
53 Norris DJ, Sacra A, Murray CB, Bawendi MG. *Phys Rev Lett* 1994; **72**: 2612.
54 Hoheisel W, Colvin VL, Johnson CS, Alivisatos AP. *J Chem Phys* 1994; **101**: 8455.
55 de Oliveira CRM, de Paula AM, Plentz Filho FO, Medeiros Neto JA *et al. Appl Phys Lett* 1995; **66**: 439.
56 Rodrigues PAM, Tamulaitis G, Yu PY, Risbud SH. *Solid State Commun* 1995; **94**: 583.
57 Norris DJ, Bawendi MG. *Phys Rev B*, 1996; **53**: 16338.
58 Grigoryan GB, Kazaryan EM, Efros AlL, Yazeva TV. *Sov Phys Solid State* 1990; **32**: 1031.
59 Vahala KJ, Sercel PC. *Phys Rev Lett* 1990; **65**: 239.
60 Sercel PC, Vahala KJ. *Phys Rev B* 1990; **42**: 3690.
61 Koch SW, Hu YZ, Fluegel B, Peyghambarian N. *J Crystal Growth* 1992; **117**: 592.
62 Efros AlL. *Phys Rev B* 1992; **46**: 7448.

63 Efros AlL, Rodina AV. *Phys Rev B* 1993; **47**: 10005.
64 Takagahara T. *Phys Rev B* 1993; **47**: 4569.
65 Nomura S, Segawa Y, Kobayashi T. *Phys Rev B* 1994; **49**: 13571.
66 Chamarro M, Gourdon C, Lavallard P, Ekimov AI. *Jpn J Appl Phys* 1995; **34**: (Suppl 34-1): 12.
67 Kochereshko VP, Mikhailov GV, Ural'tsev IN. *Sov Phys Solid State* 1983; **25**: 439.
68 Henry CH, Nassau K. *Phys Rev B* 1970; **1**: 1628.
69 Nirmal M, Murray CB, Bawendi MG. *Phys Rev B* 1994; **50**: 2293.
70 Bawendi MG, Carroll PJ, Wilson WL, Brus LE. *J Chem Phys* 1992; **96**: 946.
71 O'Neil M, Marohn J, McLendon G. *J Phys Chem* 1990; **94**: 4356.
72 Eychmüller A, Hässelbarth A, Katsikas L, Weller H. *Ber Bunsenges Phys Chem* 1991; **95**: 79.
73 Hässelbarth A, Eychmüller A, Weller H. *Chem Phys Lett* 1993; **203**: 271.
74 Calcott PDJ, Nash KJ, Canham LT, Kane MJ, Brumhead D. *J Lumin* 1993; **57**: 257.
75 Calcott PDJ, Nash KJ, Canham LT, Kane MJ, Brumhead D. *J Phys Condens Matter* 1993; **5**: L91.
76 Hybertsen MS. *Phys Rev Lett* 1994; **72**: 1514.
77 Schmitt-Rink S, Miller DAB, Chemla DS. *Phys Rev B* 1987; **35**: 8113.
78 Haynes JR, Lax M, Flood WF. *Proc Int Conf Semicond Phys Prague* 1961; **423**.
79 Cuthbert JD. *Phys Rev B* 1970; **1**: 1552.
80 Canham LT. *Appl Phys Lett* 1990; **57**: 1046.
81 Koyama H, Araki M, Yamamoto Y, Koshida N. *Jpn J Appl Phys* 1991; **30**: 3606.
82 Lehmann V, Gösele U. *Appl Phys Lett* 1991; **58**: 856.
83 Petrova-Koch V, Muschik T, Kux A, Meyer BK, Koch F, Lehmann V. *J Appl Phys* 1992; **61**: 943.
84 Lehmann V, Gösele U. *Adv Mater* 1992; **4**: 114.
85 Halimaoui A, Oules C, Bomchil G *et al. Appl Phys Lett* 1991; **59**: 304.
86 Bressers PMMC, Knapen JWJ, Meulenkamp EA, Kelly JJ. *Appl Phys Lett* 1992; **61**: 108.
87 Bsiesy A, Muller F, Ligeon M *et al. Phys Rev Lett* 1993; **71**: 637.
88 Ligeon M, Muller F, Herino R *et al. J Appl Phys* 1993; **74**: 1265.
89 Kooij ES, Despo RW, Kelly JJ. *Appl Phys Lett* 1995; **66**: 2552.
90 Littau KA, Szajowski PF, Muller AJ, Kortan RF, Brus LE. *J Phys Chem* 1993; **97**: 1224.
91 Wilson WL, Szajowski PF, Brus LE. *Science* 1993; **262**: 1242.
92 Schuppler S, Friedman SL, Marcus MA *et al. Phys Rev Lett* 1994; **72**: 2648.
93 Brus L, Szajowski P, Wilson W, Harris T, Schuppler S, Citrin P. *J Am Chem Soc* 1995; **117**: 2915.
94 Schuppler S, Friedman SL, Marcus MA *et al. Phys Rev B* 1995; **52**: 4910.
95 Suemoto T, Tanaka K, Nakajima A, Itakura T. *Phys Rev Lett* 1993; **70**: 3659.
96 Suemoto T, Tanaka K, Nakajima A. *J Phys Soc Jpn* 1994; **63** (Suppl B): 1900.
97 Takagahara T, Takeda K. *Phys Rev B* 1992; **46**: 15578.
98 Proot JP, Delerue C, Allan G. *Appl Phys Lett* 1992; **61**: 1948.
99 Delley B, Steigmeier EF. *Phys Rev B* 1993; **47**: 1397.
100 Yablonovitch E, Allara DL, Chang CC, Gmitter T, Bright TB. *Phys Rev Lett* 1986; **57**: 249.
101 Tolbert SH, Herhold AB, Johnson CS, Alivisatos AP. *Phys Rev Lett* 1994; **73**: 3266.
102 Johansson KP, McLendon GP, Marchetti AP. *Chem Phys Lett* 199; **179**: 32.
103 Johansson KP, Marchetti AP, McLendon GP. *J Phys Chem* 1992; **96**: 2873.
104 Marchetti AP, Johansson KP, McLendon GP. *Phys Rev B* 1993; **47**: 4268.
105 Chen W, McLendon G, Marchetti A, Rehm JM, Freedhoff M, Myers C. *J Am Chem Soc* 1994; **116**: 1585.
106 Kanzaki H, Tadakuma Y. *Solid State Commun* 1991; **80**: 33.
107 Babic D, Tsu R, Greene RF. *Phys Rev B* 1992; **45**: 14150.
108 Tsu R, Babic D. *Appl Phys Lett* 1993; **64**: 1806.
109 Delerue C, Allan G, Lannoo M. *Phys Rev B* 1993; **48**: 11024.
110 Lannoo M, Delerue C, Allan G. *Phys Rev Lett* 1995; **74**: 3415.

111 Chazalviel J, Ozanam F, Dubin V. *J Phys I France* 1994; **4**: 1325.
112 Martin E, Delerue C, Allan G, Lannoo M. *Phys Rev B* 1994; **50**: 18258.
113 Brus LE. *Phys Rev B* 1996; **53**: 4649.
114 Marcus R. *J Chem Phys* 1956; **24**: 966.
115 Marcus R. *Faraday Disc Chem Soc* 1960; **29**: 21.
116 Miller RJD *et al. Surface Electron Transfer Processes*. New York: VCH Publishers, 1995: Chs 1, 4.
117 O'Regan B, Gratzel M. *Nature* 1991; **353**: 737.
118 Colvin V, Schlamp M, Alivisatos AP. *Nature* 1994; **370**: 6488.
119 Dabbousi B, Bawendi M, Onitsuka O, Rubner M. *Appl Phys Lett* 1995; **66**: 1316.
120 Wang Y, Herron N. *Chem Phys Lett* 1992; **200**: 71.